Localized Baroclinicity: A Source for Meso-α Cyclones

ISIDORO ORLANSKI

Geophysical Fluid Dynamics Laboratory/NOAA, Princeton University, Princeton, NJ 08542

ABSTRACT

An investigation has been made using a two-dimensional model to solve the initial value problem describing the evolution of disturbances on a mean baroclinic state. Three main problems are considered:

1) the effect of static stability on meso-baroclinic waves in a periodic domain;
2) downstream instability in an open domain and the effect of surface sensible heat; and
3) the effect of moisture on these unstable waves.

It was found that a flow can be unstable to mesoscale baroclinic waves. The requirement for instability of wavelengths less than 1000 km is similar to that for the planetary quasi-geostrophic baroclinic waves. The Rossby penetration height, $\delta = fL/N$, can be derived from the solution of the unstable waves as

$$\delta \approx -|u - c|^2 \bigg/ 2\frac{du}{dz}(u - c_r);$$

these unstable waves will only be sensitive to the baroclinicity of the atmosphere in a layer with a depth δ.

The characteristics of the finite amplitude unstable waves suggest that the limiting amplitude for the baroclinic waves is achieved by an energy cascade to frontal scales.

Perhaps the most significant finding of this study has been to demonstrate the importance of localized surface heating in producing the more intense development of short baroclinic waves. It was found that waves in the presence of surface heating grew twice as fast as those without. These waves, having a depth on the order of the boundary layer and horizontal scales ($L \approx N\delta/f$) of a few hundred kilometers, can organize convergence of surface moisture on these scales. With the addition of moisture, the shallow meso-baroclinic wave will explosively develop into a deep intense system.

1. Introduction

One facet of mesoscale research in recent years has been the detailed analysis of "explosive cyclogenesis" in winter storms, (Sanders and Gyakum, 1980), such as the Polar low (Reed, 1979; Rasmussen, 1979; Rasmussen, 1981), comma clouds (Reed, 1979; Mullen, 1979; Mullen, 1983) and coastal cyclogenesis (Bosart, 1981; Uccellini et al., 1984). The conclusion which these studies all have in common is that baroclinicity of planetary waves, latent heating and surface heating are all important to the development of subsynoptic winter storms. In a recent study on the predictability of mesoscale phenomena (Orlanski and Polinsky, 1984) in which numerical simulations of winter storms had been performed, specifically on coastal cyclogenesis and a comma cloud among others, it was concluded that the most important mechanism needed to nurture the characteristic explosiveness of these storms is latent heat release from condensation. However, it is not clear what the triggering mechanism is for such systems. A surprising feature of these studies is that weak meso-α cyclones[1] develop for the dry simulations in approxi-

mately the same geographical position as those simulations having latent heat release; this suggests that the dry atmosphere may have the necessary ingredients for the development of meso-α cyclones, and that latent heat makes its development explosive. Accordingly, observations suggest strong baroclinicity and considerable surface sensible heating, implying that the rather warm ocean in the middle to high latitudes could provide a large source of sensible heat to the very cold air masses. Bosart and Lin (1984), using a coastal cyclogenesis situation (the President's Day Snowstorm), have shown that the sensible heat from the ocean surface is very large and accounts for about one-third of the total surface heat release. Similar findings were reported concerning the development of polar lows in the North Atlantic (Rasmussen, 1979). In the numerical simulation of the mid-Pacific comma cloud (Orlanski and Polinsky, 1984), it was found that the environment of the lower atmosphere, from the ocean surface to about 750 mb, had a very weak static stability and a rather small Richardson number (Ri ≈ 1) prior to the development of the comma cloud. Collectively, this suggests that the baroclinic flow encounters an area of

---

[1] We refer to the meso-α cyclone as a subsynoptic cyclone with an approximate scale of 500 km in an effort to distinguish it from the term mesocyclone found in the literature associated with severe storms.

weak static stability in the lower layers of the atmosphere above the ocean. One can further speculate that very shallow waves will be excited under such conditions (Reed, 1979; Blumen, 1979). The purpose of this paper, then, will be to investigate the stability of flows with localized baroclinicity characteristic of conditions that might lead to explosive cyclogenesis.

In section 2 we will describe the stability characteristics of a baroclinic flow and its dependence on various stratifications for periodic disturbances. Section 3 will deal with the nonlinear behavior of these unstable waves. The stability of isolated disturbances along with the effect of localized heating and its time averaged heat budgets will be treated in section 4. Finally, we will consider the effect of moisture on those disturbances in section 5.

2. The role of stratification in the stability of baroclinic flows

The role of static stability in the development of short baroclinic waves has been studied extensively (Gall, 1976a; Staley and Gall, 1977; Blumen, 1979) in the framework of quasi-geostrophic models or general circulation models (GCM) that have a rather coarse horizontal resolution. All of these studies suggested that the low static stability of the lower atmosphere is supportive of shallow, short baroclinic waves.

Moreover, the observational evidence of strong meso-α cyclone development under low static stability conditions can be seen in a numerical simulation of the evolution of a comma cloud. (A summary is given in Orlanski and Polinsky, 1984). This study, the details of which will be published elsewhere, deals with the sensitivity of the moisture content to the quality of the simulation for three-dimensional numerical simulations of an observational case beginning on 11 January 1979 with a widespread frontal system in the eastern Pacific. For that purpose, each simulation was performed with a different moisture initialization; that is: observed moisture, zero moisture or enhanced moisture. At the initial time a small shallow disturbance occurs behind the front with weak vorticity. Within the next 24 h of the simulation the small disturbance intensifies, generating considerable vorticity that develops to form an apparent comma shape centered at about (45°N, 150°W).

Figure 1 shows a comparison of the vertical component of relative vorticity at the surface for 24, 36 and 48 h into the simulation. The shaded areas denote regions of relative vorticity larger than 2.5×10^{-5} s^{-1}. At 36 h (middle row), note the different intensities of the vorticity between (a) a dry environment, (b) the observed moisture, and (c) enhanced moisture. Our interest here, however, will be focused on the extremely similar position of the vortices in these solutions. This basically suggests that although the latent heat in solutions (b) and (c) intensified, the vortex cen-

ters, as previously suggested (Nitta and Ogura, 1972; Gambo, 1970; Gall, 1976b), already existed in the dry environment, solution (a). Let us first examine the mechanisms that organize vorticity on such scales. Upon inspecting the Richardson numbers of the initial conditions which generated the dry solution (a) of Fig. 1, one notices large pockets of Richardson number, the order of unity and smaller, located where the vortices eventually form (see Fig. 2). Richardson numbers shown in Fig. 2 are limited to the lower layers from the surface to about 1000 m. Temperature soundings also analyzed for those cases corroborate the fact that the lower layers of the atmosphere are characterized by low static stability. These results suggest that a baroclinic flow in the presence of shallow low static stability may generate unstable waves with short (mesoscale) wavelengths. Let us review then possible mechanisms for generating unstable waves in a baroclinic model.

a. The Eady model

In the most simple baroclinic model of Eady (1949), with constant vertical wind shear and rotation, unstable waves develop which have a growth rate depending on

$$C_i = \frac{H}{\mu} \frac{d\bar{u}}{dz} [(\mu - \tanh\mu)(\coth\mu - \mu)]^{1/2},$$

$$C_i \neq 0 \quad \text{for} \quad \mu < \mu_c = 1.1997 \qquad (2.1)$$

where

$$\mu = (k^2 + l^2)^{1/2} \frac{NH}{2} \Big/ f,$$

with k and l the nondimensional horizontal wavenumbers; N is the Brunt Väisälä frequency; H is the height of the atmosphere, and f is the Coriolis parameter.

We can see that the growth rate increases with the shear; however, the maximum wavelength of the unstable waves and the critical wavenumber where the system becomes unstable for this quasi-geostrophic model do not depend on the vertical shear, $\mu_c \neq f(d\bar{u}/dz)$, but rather is proportional to NH/f. This ratio of NH/f to the horizontal wavenumber length, λ, is actually Ro (Rossby number Ro $= U_0/fL$) and the Ri$^{1/2}$ Richardson number Ri $\equiv N^2H^2/U_0^2$ in which the Richardson number has been defined with a dimensional vertical shear of U_0/h and does not depend on the actual shear, du/dz. Furthermore, the Burger number, B, which is Ro^{2}Ri, defines the ratio of the slope of the particle trajectories of the waves (w/v) to the slope of the isentropes (θ_y/θ_z) in a quasi-geostrophic regime where, due to the continuity equation,

$$w \approx O\left(\text{Ro} \frac{H}{L} V\right).$$

This result can easily be extended to the nongeostrophic regime up to Ro ≈ 1 (see Orlanski and Cox, 1973). It

PACIFIC POLAR LOW EXP. VORTICITY AT THE SURFACE (Z = 0)

Jan 12 0000 Z (24hrs.)

No Moisture   Observed Moisture (FGGE)   Enhanced Moisture (if r > 50%; r = 90%)

Jan 12 1200 Z (36hrs.)
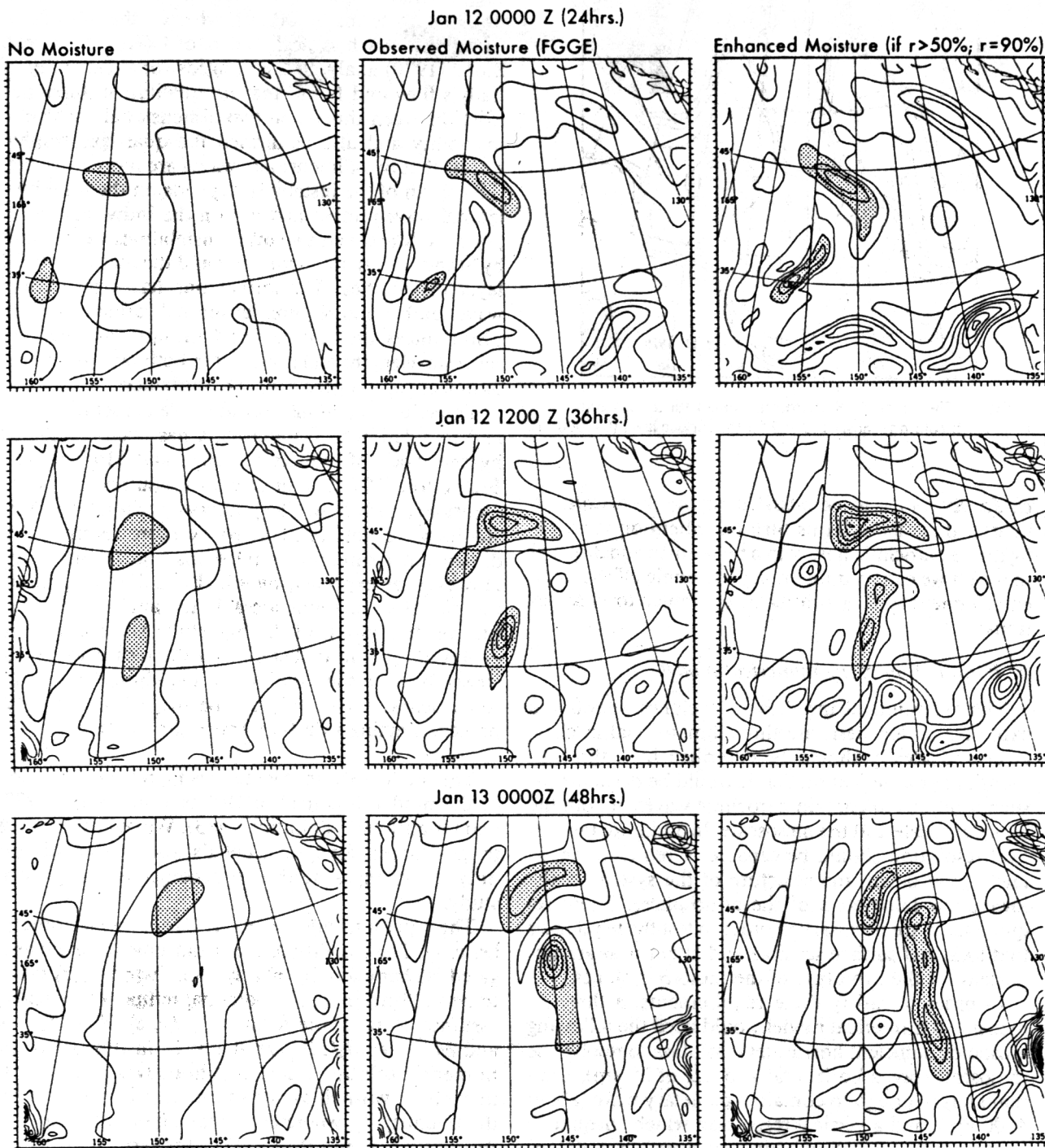
Jan 13 0000Z (48hrs.)

FIG. 1. A comparison of the vertical component of vorticity at the surface for 24, 36 and 48 h of the comma cloud solution. The dry, observed, and enhanced moisture solutions are shown from left to right respectively. Contours are shown at intervals of 2.5×10^{-5} s^{-1} with the shaded areas representing regions of relative vorticity greater than 2.5×10^{-5} s^{-1}.

is well known that the Eady model, being quasi-geostrophic, implies that Ro ≪ 1 and Ri ≫ 1. If baroclinic instability can operate on the mesoscale, we should find that particle trajectories have slopes similar to that of the isentropes, so that B ≈ O(1). Certainly for those scales, however, we do not expect that the system will be quasi-geostrophic or that Ro ≪ 1. *In fact, Ro ≈ 1 which necessitates that Ri ≈ 1 as a condition for baro-*
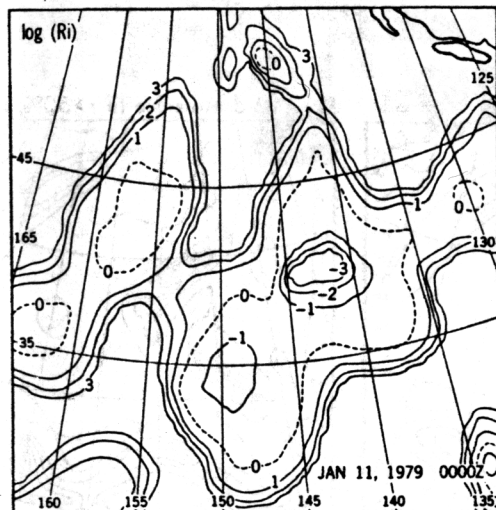
FIG. 2. The log of the Richardson number for the dry solution (Fig. 1, left column) shown at $t = 0$ for the surface layer (0–1000 m).

clinic instability to be possible on the mesoscale. In light of these facts, let us turn our attention to investigating a baroclinic flow with a two-dimensional model in which we can examine nongeostrophic effects in an environment with a stratification similar to observations.

b. Formulation of the numerical model

The evolution of the meso-α cyclones relevant to explosive cyclogenesis are three-dimensional in character and ideally should be described by a three-dimensional numerical model. It would be desirable for such solutions to contain baroclinic waves in both the planetary scale and the mesoscale. In addition, the vertical resolution should be capable of representing, in fairly good detail, the structure of the system in the lowest few kilometers of the atmosphere. These requirements are necessary in order to test the hypothesis that localized surface sensible and latent heat are important for the evolution of the meso-α cyclones.

In order to satisfy these requirements, a three-dimensional numerical model would need the following attributes: sufficient horizontal resolution to resolve the mesoscale (say, a horizontal grid size of 25 km), a domain large enough to contain a planetary wave (about 4000 km), and a vertical resolution which adequately represents the planetary boundary layer ($\Delta z = 300$ m) and is still able to reach the tropopause ($H = 18$ km). Clearly such a model would be very expensive to use.

The stability of idealized baroclinic flows, such as in the Eady (1949) model, has shown that, at least in the quasi-geostrophic approximation, two-dimensional disturbances (no latitudinal variation of the perturbation) have the maximum growth rates, and they are not qualitatively different from their three-dimensional counterparts. Phillips (1964) cautions against neglecting the latitudinal variation of the perturbations in the sta-

bility of nongeostrophic baroclinic flows; his paper suggests that the linearized nongeostrophic Eady equations retain terms of $O(Ro^2)$, whereas the latitudinal variability which is neglected is of $O(Ro)$. However, Stone (1970) analyzed the nongeostrophic stability of Eady's flow and found that no qualitative difference exists between three- and two-dimensional baroclinic instability and also confirmed the quasi-geostrophic results that two-dimensional waves are more unstable; the growth of the instability depends on the total horizontal wavenumber and not on the individual components. Moreover, two other instabilities were found by Stone (1970): the symmetric and the inertial critical layer instabilities. The former one has a zero zonal wavenumber and requires latitudinal variability of the disturbances; on the other hand, the latter one has very short wavelengths and is present in both two- and three-dimensional nongeostrophic disturbances.

The solution of nonlinear unstable baroclinic waves and its relation to frontogenesis has been elucidated by the work of Williams (1967) and Hoskins and Bretherton (1972), both of which assumed a two-dimensional Eady flow. The primary conclusions of these studies were not contradicted by more recent three-dimensional simulations (Hoskins and West, 1979). However, as expected, only high resolution three-dimensional simulations are able to capture the quantitative description of the baroclinic wave and front evolution. It is in that spirit that the results to be discussed here on the evolution of two-dimensional meso-baroclinic waves only can be suggestive of similar processes acting in a fully three-dimensional meso-α cyclone.

The model used in this study is merely an extension of the model described in Orlanski and Ross (1977) and Orlanski and Polinsky (1983). We refer the reader to these papers for specific details, and we shall discuss only the changes needed to accomplish the present study.

The equations are written in Cartesian coordinates (x, y, z). The stability of the mean flow to be investigated is characterized by a synoptic wind $U_g(z)$ taken to be uniform in x. The potential temperature field is assumed to be of the form $\theta + \theta_g(y, z)$ where $\theta_g = 0$ and $\partial \theta_g / \partial y = f \theta_0 / g \partial U_g / \partial z$ at $y = 0$. In this paper the numerical solution is assumed to be two-dimensional in x and z with all variables uniform in y except for the quantity θ_g, where $\partial \theta_g / \partial y$ is only a function of z. As in Orlanski and Ross (1977), the term $\partial \theta_g / \partial z$ is neglected compared to $\partial \theta / \partial z$ in the vertical advection of heat. Note that, if $U(z)$ is a linear function of z as in the Eady flow, the term $\partial \theta_g / \partial z$ ($\partial \theta_g / \partial z \propto \partial^2 U_g / \partial z^2$) is absolutely zero. The term θ_{gz} can be shown to be small compared with the mean lapse rate if the curvature of the flow is small.[2]

---

[2] For $\theta_{gz} < \theta_z$, since it is in geostrophic balance $\left| \dfrac{-f \theta_0}{g} U_{gzz} y \right| < \theta_z$

and for that relation to be valid, L_y, the meridional scale of the dis-

Table 1 - EXPERIMENTS

Boundaries	Periodic													Open									
Wavelength (km)	1000	1000	1250	1500	1500	1750	2000	2000	2500	2500	3500	3500	3500	450	450	450	450	450	450	700	700	1000	1000
Stratification High = N_H = 4 c/km		x	x		x	x		x	x	x	x		x	x	x	x	x	x	x	x	x	x	x
Low = N_L = 1 c/km	x			x			x						x										
Shear High = S_H = 14 m s⁻¹		x			x		x		x		x		x	x	x				x				
Low = S_L = 8 m s⁻¹	x		x	x		x	x		x			x	x			x	x	x		x	x	x	x
Domain Length (km)	1000	1000	1250	1500	1500	1750	2000	2000	2500	2500	3500	3500	3500	4000	4000	4000	4000	4000	4000	4000	4000	4000	4000
Height (km)	16	16	16	16	16	16	16	16	16	16	16	16	16	16	16	16	16	16	16	16	16	16	16
Δx (km)	16.6	16.6	20.8	25	25	29.2	33.3	33.3	41.7	41.7	58.3	58.3	58.3	25	25	25	25	25	25	25	25	25	25
Δz (m)	1000	1000	1000	1000	1000	1000	1000	1000	1000	1000	1000	1000	1000	333	333	333	333	333	333	333	333	333	333
N_{SPC}	No	No	No	No	No	No	No	No	No	No	No	No	No	No	Yes	No	Yes	Yes	Yes	Yes	No	Yes	No
Moisture	No	No	No	No	No	No	No	No	No	No	No	No	No	No	No	No	No	Yes	Yes	No	No	No	No

We retain the v velocity for rotational effects. Then using the set of equations as given in Orlanski and Ross (1977), we define our nonlinear set of equations as

$$\frac{\partial \zeta}{\partial t} - J(\psi, \alpha_0 \zeta) = f\frac{\partial v}{\partial z} - \frac{g}{\theta_0}\frac{\partial \theta}{\partial x} + \frac{\partial}{\partial x}\left(K\nu_e\frac{\partial \zeta}{\partial x}\right) + \frac{\partial}{\partial z}\left(\nu_e\frac{\partial \zeta}{\partial z}\right),$$

(2.2)

$$\frac{\partial v}{\partial t} - \alpha_0 J(\psi, v)$$

$$= -f\left(\alpha_0\frac{\partial \psi}{\partial z} - U_g\right) + \frac{\partial}{\partial x}\left(K\nu_e\frac{\partial v}{\partial x}\right) + \frac{\partial}{\partial z}\left(\nu_e\frac{\partial v}{\partial z}\right),$$

(2.3)

$$\frac{\partial \theta}{\partial t} - \alpha_0 J(\psi, \theta) + v\frac{\partial \theta_g}{\partial y} = \frac{\partial}{\partial x}\left(K\kappa_e\frac{\partial \theta}{\partial x}\right) + \frac{\partial}{\partial z}\left(\kappa_e\frac{\partial \theta}{\partial z}\right),$$

(2.4)

where U_g and θ_g are the prescribed geostrophic basic flow and where ζ is the "y" vorticity component ($u_z - w_x$), u, v and w are the x, y and z component of the wind, respectively, and θ is the potential temperature. The vorticity as a function of the streamfunction is

$$\zeta = \alpha_0\frac{\partial^2 \psi}{\partial x^2} + \frac{\partial}{\partial z}\left(\alpha_0\frac{\partial \psi}{\partial z}\right),$$

(2.5)

where α_0 is the specific volume, defined as $\alpha_0 = 1/\rho_0$. The Jacobian is defined as

$$J(A, B) = \frac{\partial A}{\partial x}\frac{\partial B}{\partial z} - \frac{\partial A}{\partial z}\frac{\partial B}{\partial x}.$$

(2.6)

---

turbance, should be $L_y < \frac{N^2}{fU_{gzz}} \approx \frac{N^2 H^2}{fU_0}$. For typical values used in this study, this inequality is satisfied when $L_y < 10^4$ km.

Studies have shown that the hydrostatic assumption is a good approximation where the horizontal velocities are much larger than vertical velocities. This assumption is also computationally more economical than the ADI (alternating direction implicit) method of solving the Poisson equation; therefore, if we utilize this assumption, Eq. (2.5) becomes

$$\zeta = \frac{\partial}{\partial z}\left(\alpha_0\frac{\partial \psi}{\partial z}\right);$$

(2.7)

ν_e and κ_e are the nonlinear eddy viscosity and diffusivity respectively, while K is the ratio of horizontal to vertical viscosity coefficients (see Table 1 for specific details). Their formulation depends on the local static stability (see the Appendix for a more complete discussion). We should mention that values of Δt, f and K (180 s, 10^{-4} s⁻¹ and 1000, respectively) were the same for all experiments.

c. Initial conditions

The mean state in which the disturbances develop is characteristic of the standard atmosphere. Basically, we use two potential temperature profiles or a combination of these (Fig. 3). The N_L designates the profile having a low stratification (1°C km⁻¹) in the troposphere (below 11 km), while N_H defines the profile of high stratification (4°C km⁻¹) in the troposphere. Both profiles have the high stratification characteristic of the lower stratosphere. Hyperbolic tangents were used for the wind profiles with two different shears considered, one with a maximum of 8 m s⁻¹ at 10 km (S_L) and the other with a maximum of 14 m s⁻¹ at 10 km (S_H). A profile of the characteristic Richardson number

$$\text{Ri} = \frac{N^2}{(du/dz)^2}$$

for S_L and N_H is also shown in Fig. 3. The initial perturbation v-velocity is assumed to be at

$$V = V_0 \cos \frac{\pi}{H} z \cos \frac{2\pi}{L} x, \qquad (2.8)$$

where $V_0 = 2$ m s^{-1} and L, the length of the channel, is case dependent.

d. The periodic solution

Several numerical integrations using various combinations of the initial conditions were performed using periodic conditions in the x-direction. Figure 4 shows a time sequence (initial, 96, 192 and 288 h) of the v-velocity as a function of x and z; this particular case had a channel length, L, equal to 2500 km ($\Delta x \sim 40$ km), a height H equal to 16 km ($\Delta z = 1$ km), high shear (S_H), and high stratification (N_H). In fact, the solution corresponds to the most unstable wave for that environment as we can see after 96 h of integration. Since the system of equations is nonlinear, the baroclinically unstable wave grows to an amplitude of 60 m s^{-1} at 192 h and exhibits a frontal development at the surface similar to that described by Williams (1967) and Hoskins and Bretherton (1972). This pattern is maintained throughout the integration with the unstable wave achieving an amplitude of close to 80 m s^{-1} at 288 h. The evolution of the finite amplitude wave and its associated frontal structure will be discussed in a later section.

The growth rate over the first few days is fairly constant and can be described by linear theory. The doubling time, the time in which the amplitude doubles, was calculated from the time evolution of the maximum amplitude of the waves. The initial amplitude for this calculation was taken at a time subsequent to the initiation of the integration, in order to avoid contamination due to the initial transients. The calculated doubling time is shown for the different experiments as a function of wavelength in Fig. 5. The upper curve corresponds to a high stratification, low shear case (N_H, S_L). The doubling time of 52 h corresponds to a 2500-km wave; for the same stratification with increased shear (S_H), the doubling time is halved to about 25 h. The maximum unstable waves for S_L and S_H are the same as one might expect from Eady's result, namely that a change in the shear will alter the growth rate but not the wavenumber of the most unstable wave. If we now reduce the stratification, say for the low stratification N_L and low shear S_L (Fig. 3), we notice that the doubling time has decreased to half the value of the (N_H, S_L) case as reflected in Eq. (2.1), and the most unstable waves have moved to shorter wavelengths.

e. Sensitivity to stratification

The structure of a wave with a characteristic wavelength of 1000 km for weak shear with high or low stratification is shown respectively in the upper and middle left cross section of Fig. 6 for $t = 336$ h. The corresponding mean potential temperature profile (the horizontal mean of the initial θ field) is shown to the right of each cross section. The wave amplitude in the N_L case is much larger than the corresponding N_H case.

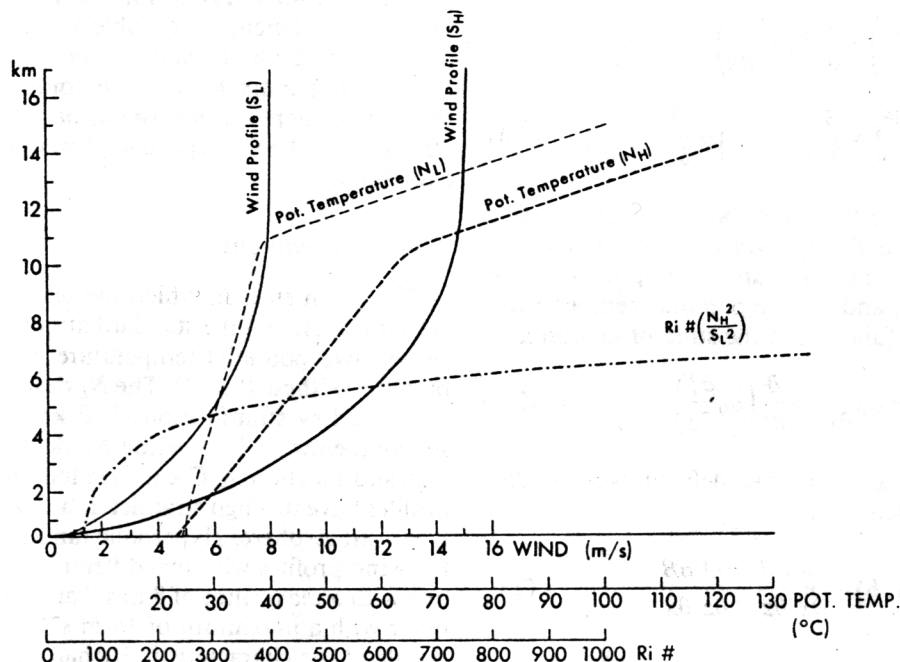
FIG. 3. Profiles showing the potential temperature for the N_L (low) and N_H (high) stratifications, wind profiles for S_L (low shear) and S_H (high shear), and a profile of the characteristic Richardson number.
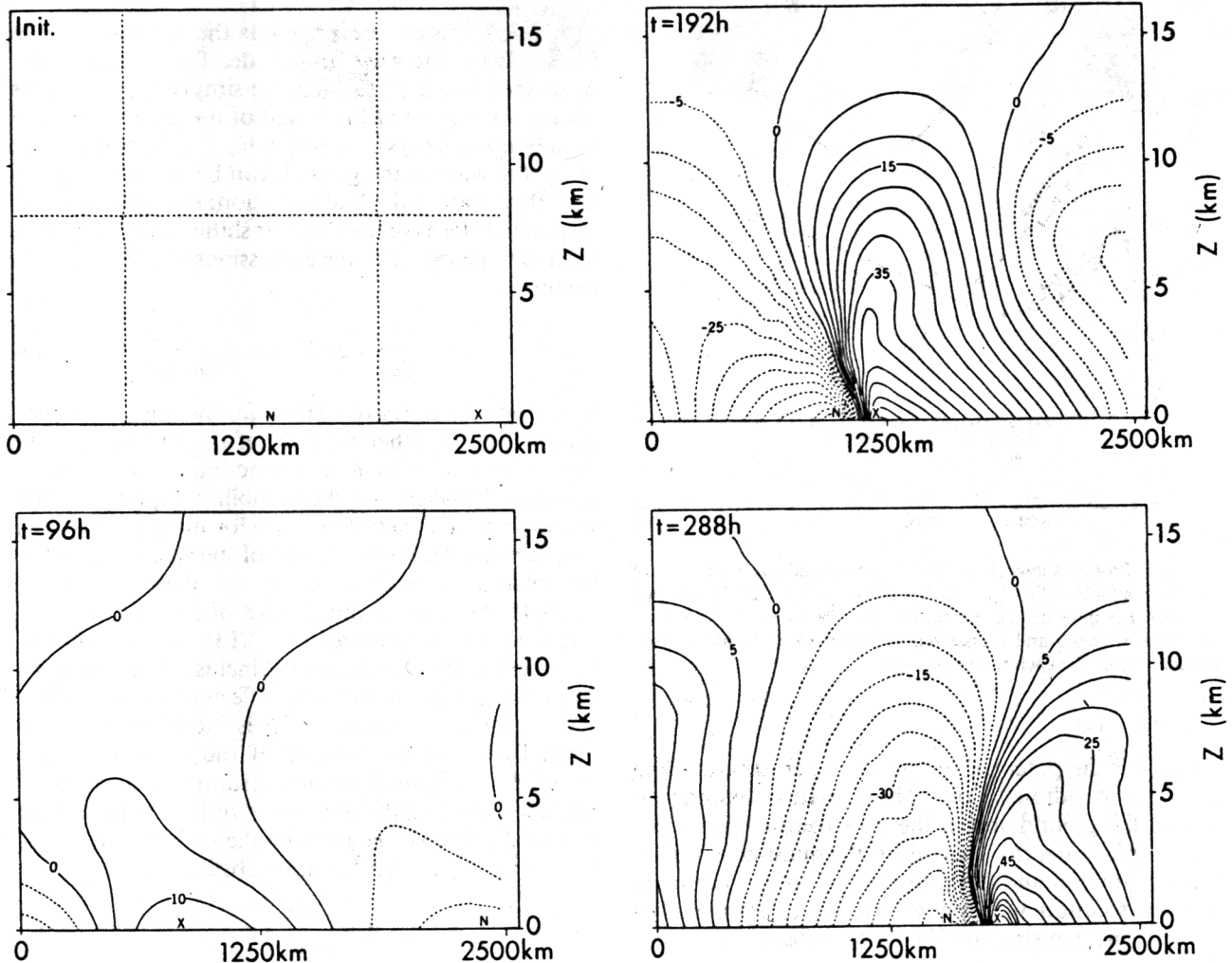
N_H, S_H (periodic)   V-velocity   (2500km)

FIG. 4. Cross sections of the v-velocity (m s^{-1}) as a function of x and z shown at $t = 0, 96, 192$ and 288 h for an N_H, S_H case with a 2500-km wave imposed on a domain with lateral periodic boundary conditions.

The doubling time from Fig. 5 is 25 h for the N_L case and close to 90 h for the N_H case. We can also notice that the vertical penetration of these short waves is relatively shallow, and most of the structure is below 5 km. That is an important fact for the scale selection of the unstable waves in baroclinic shallow layers such as over the ocean where, due to sensible heat release, the stratification of layers can be considerably reduced. To study such cases we can use a profile that is modified to include the N_L profile in the lower layers, below 4 km, with the N_H profile throughout the rest of the troposphere. This case (designated as N_H/N_L) is shown in the lower part of Fig. 6. If this solution is compared to the middle solution of Fig. 6, one finds that the structure of this unstable wave, (N_H/N_L), is quite similar in the lower levels of the atmosphere where the entire troposphere is characterized by low static stability. A similar result was found by Blumen (1979, 1980) in which a two-layer stratified fluid was considered. The

long borelike wave occupied the entire atmosphere. Short baroclinic waves, however, occupied the lower layer with weaker stratification. He showed that long and short baroclinic waves are unstable. In fact the results suggest that the instabilities are possible as long as the atmosphere has a layer of low static stability the depth of which is greater than or equal to the depth of the unstable waves. The question then becomes, *what determines the depth of penetration for baroclinically unstable waves?*

f. Penetration depth

In the quasi-geostrophic limit, we can estimate the depth of the Eady solution if we recall that the linearized boundary condition at the ground is

$$\frac{\partial \theta}{\partial t} + \bar{u}_0 \frac{\partial \theta}{\partial x} + v \frac{\partial \bar{\theta}}{\partial y} = 0 \quad \text{at} \quad z = 0, \qquad (2.9)$$
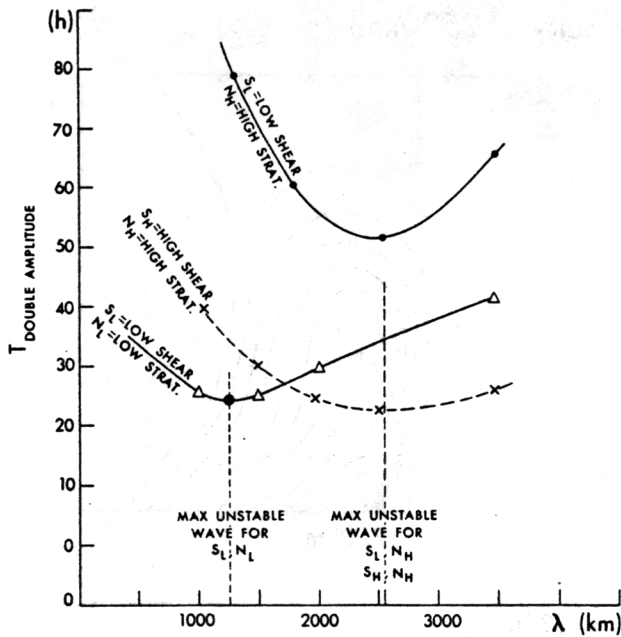
FIG. 5. Profiles showing the doubling amplitude as a function of wavelength for the (N_L, S_L), (N_H, N_H) and (N_H, S_L) cases. The dashed vertical lines indicate the maximum unstable wave for each case. The dots, triangles and crosses represent the wavelengths imposed on the domain for each respective case.

where θ is the potential temperature perturbation and v is the meridional flow. This equation assumes $w = 0$ at the ground and in the quasi-geostrophic limit, v is proportional to η_x where η is the quasi-geostrophic streamfunction and θ is proportional to η_z. Assuming a wave solution with phase velocity c, as in Eady's model, one can simplify Eq. (2.9) to the form:

$$(\bar{u}_0 - c)\eta_z - \frac{d\bar{u}}{dz}\eta = 0. \qquad (2.10)$$

If we then define the ratio δ as the penetration depth,

$$\delta = -\frac{|\eta|^2}{|\eta|_z^2}, \qquad (2.11)$$

which basically defines the vertical scale for the kinetic energy of the waves. Obviously, δ will be a function of z; however, a good estimate can be obtained by evaluating the equation at $z = 0$ since the waves are maximum there. It is possible to multiply (2.10) by the complex conjugate of the product of the streamfunction and $(\bar{u}_0 - c)$; then rearranging the terms, one finds the value of δ to be given by

$$\delta = -\frac{|\eta|^2}{|\eta|_z^2} = -\frac{|\bar{u}_0 - c|^2}{2\frac{d\bar{u}}{dz}(\bar{u}_0 - c_r)} \quad \text{at} \quad z = 0. \qquad (2.12)$$

Note that the absolute value of η/η_z in Eq. (2.10) also defines a scale for the penetration of the baroclinic waves,

$$\Lambda = \left|\frac{\eta}{\eta_z}\right| = \left|\frac{\bar{u}_0 - c}{d\bar{u}/dz}\right|. \qquad (2.13)$$

In (2.12) δ can be interpreted as the vertical scale of the square of the wave amplitude. The vertical scale, Λ, defined in Eq. (2.13), may be simply interpreted as an approximation of the height of the steering level in weakly unstable systems ($|c_i| \ll |\bar{u}_0 - C_r|$). If the value of u_0, the wind at the ground, can be set arbitrarily to $u_0 = 0$ (at least in the Eady solution; in a more general case, small effects of the Doppler shifted frequency may need to be considered), the expressions (2.12) and (2.13) become

$$\Lambda = \frac{|c_r|}{d\bar{u}/dz} \quad \text{and} \quad \delta = +\frac{c_r}{2d\bar{u}/dz}. \qquad (2.14)$$

Knowing the dispersive relation for the unstable waves, substituting in either formula of (2.14) will give the dependence of Λ or δ as a function of the external parameters that control the instability. Equation (2.14) shows that the penetration scale for the wave energy δ can be estimated by the height of the steering level, Λ; the relation $\Lambda \approx 2\delta$ is due to the definition that δ refers to the squared amplitudes of (2.12) whereas Λ refers to the amplitudes of (2.13). No restrictions have been made concerning the inclusion of curvatures of the mean wind profile or the effects of the differential earth rotation (β). In fact, if β is included, c_r will be given by the phase velocity of the Rossby wave $c_r = -\beta/(k^2 + l^2)$; furthermore, assuming that the most unstable wavelengths are of the order of the Rossby radius of deformation given by the scale height, say Λ, then $(k^2 + l^2) \simeq f^2/N^2\Lambda^2$ and substituting in (2.14),

$$\Lambda = \frac{f^2 d\bar{u}}{N^2 dz}\bigg/\beta.$$

A similar condition had been derived by Held (1982).

For characteristic values of the most unstable waves, say growth rates of one day, $c_r \approx 5$ m s^{-1}, and $d\bar{u}_0/dz = 2$ m s^{-1}/km, δ can be estimated to be of the order of 1000 m. Consequently, most short baroclinic waves will be sensitive to environmental characteristics in the first two kilometers of the atmosphere, thereby explaining the results of Fig. 6. In section 4 we shall examine the depth of penetration for different shears. Since no approximations have been made for Eqs. (2.2), (2.3), (2.4) and (2.7), the nonlinear effects of the finite amplitude baroclinic waves can be investigated.

3. Finite amplitude effects on baroclinically unstable waves

We have seen that for low static stability, N_L, the doubling time for wavelengths of 1000 km is 25 h, whereas doubling time for the 2000-km wave is about 30 h. This estimate is from the initial development of the wave (small amplitude). In Fig. 7 we display the v-velocity for the 1000-km and 2000-km waves at 96 and 336 hours. Consistent with our previous discussion,
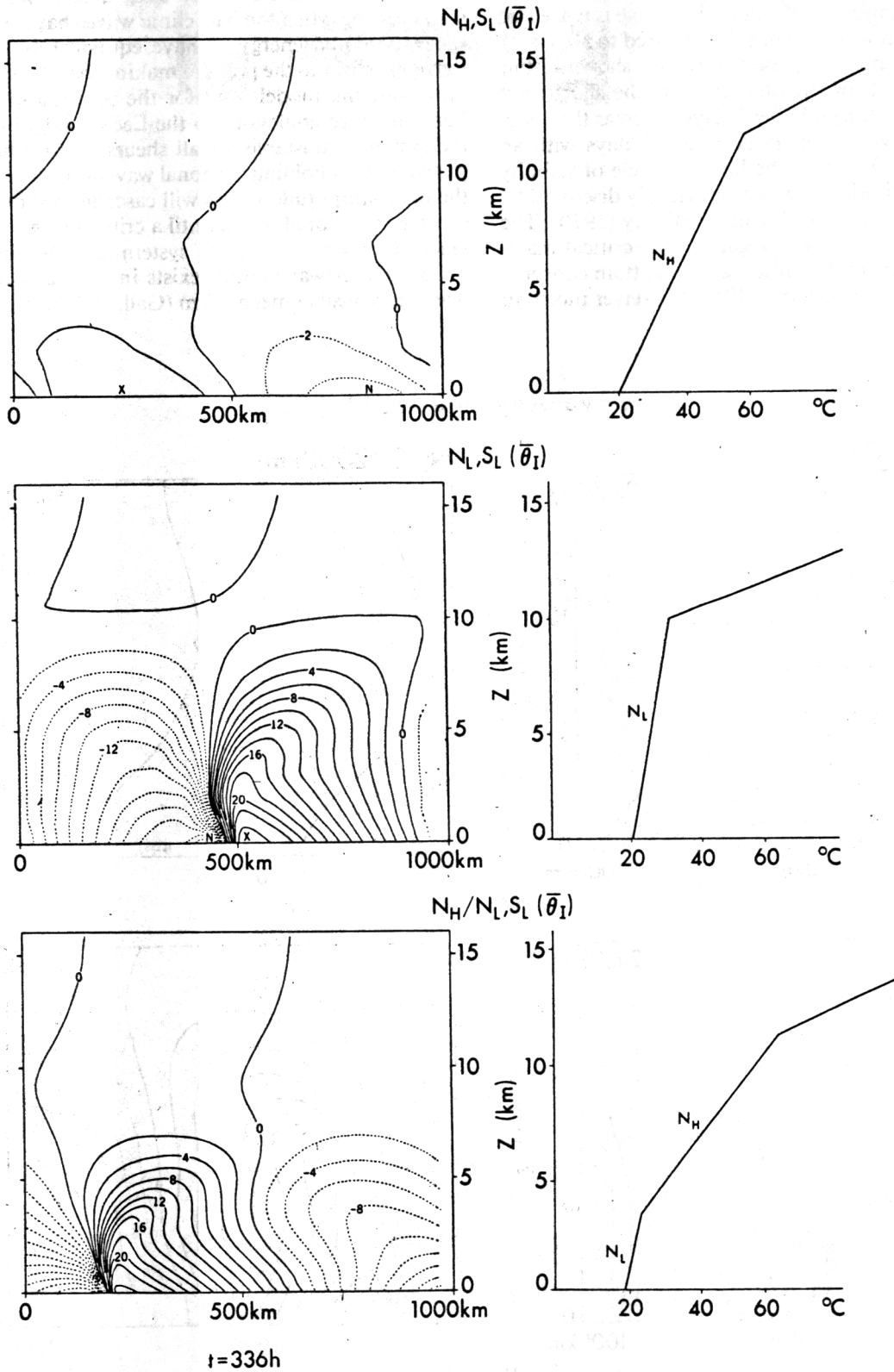
V (2m/s) (periodic) Init: Wave (1000km)

FIG. 6. Cross sections of the v-velocity (m s^{-1}) at $t = 336$ h for solutions having lateral periodic boundary conditions and an initial imposed wave of 1000 km. Solutions are shown for the (N_H, S_L), (N_L, S_L) and $(N_H/N_L, S_L)$ cases respectively with corresponding initial mean potential temperature profiles shown to the right of each cross section.

the 1000-km wave is larger in the first period of evolution (96 h) than the 2000-km wave; however, after 336 h the magnitude of the 2000-km wave is twice that of the 1000-km wave (60 m s^{-1} compared to 30 m s^{-1}). The time evolution of these two waves, shown in Fig. 8, indicates that for the first few days the short wave grows faster, leveling off after 8 days, whereas the 2000-km wave grows slower, peaking at 12 days with an amplitude of 70 m s^{-1}. The limiting cycle of stability for finite amplitude waves was previously discussed by Drazin (1978), Hart (1979) and Pedlosky (1970). The simplest explanation with regard to the critical maximum amplitude that a finite wave will attain concerns a model such as the Phillips (1954) two-layer model in

which there are critical shear layers, below which the instability does not exist. In such a case, waves will stop growing when the baroclinic waves have removed mean potential energy or have equivalently reduced the mean shear to the point of making the system stable. However, the model used for the solution shown in Fig. 7 is more analogous to the Eady model in which the system is unstable for all shears. Drazin has suggested that, by holding the zonal wavenumber constant, the finite-amplitude waves will cascade to shorter and shorter meridional scales until a critical length scale is reached, at which time the system is stable (in other words, a shortwave cutoff exists in the Eady model). Another plausible mechanism (Gall, 1976a) to stabilize
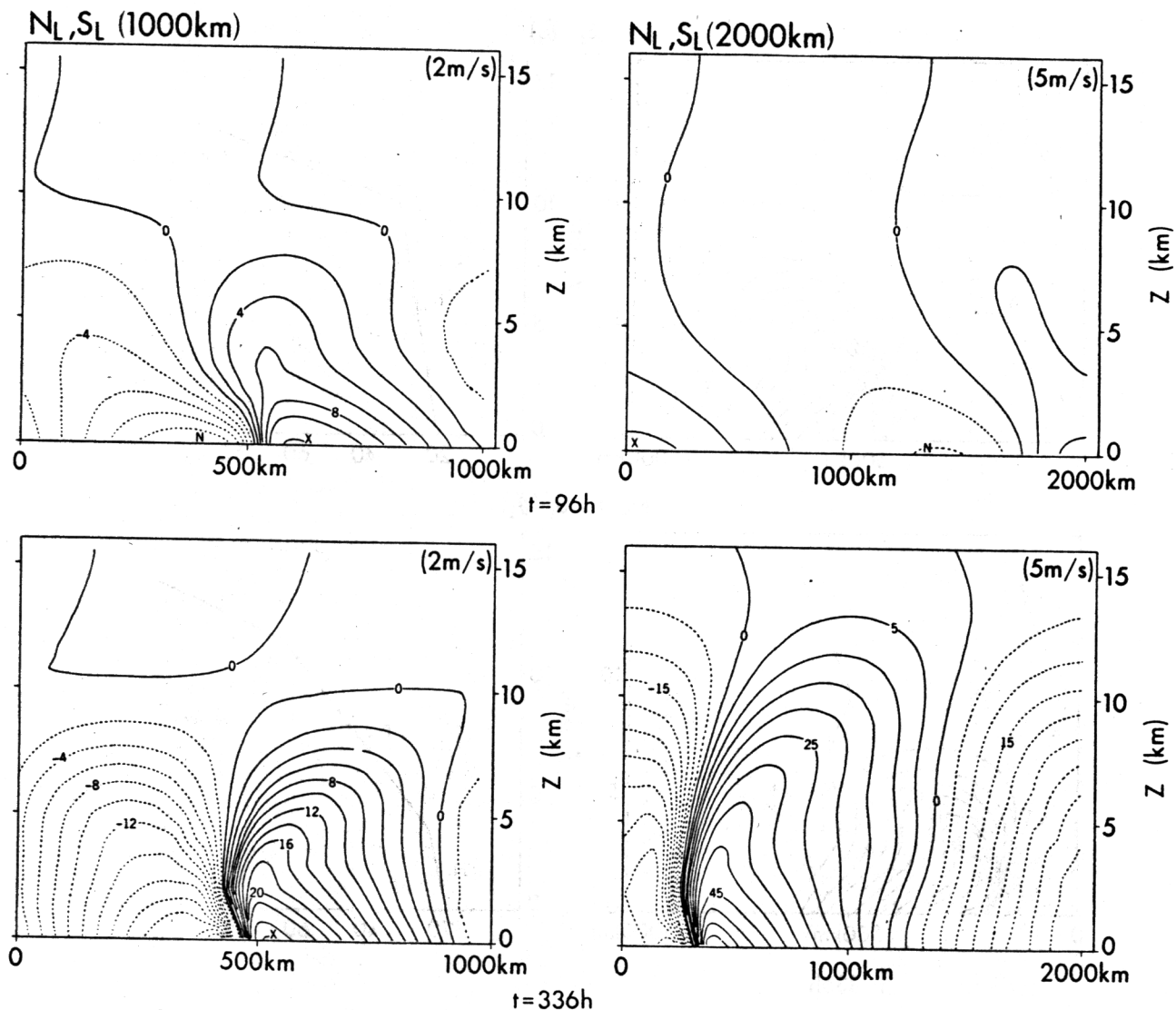

FIG. 7. A comparison of the *v*-velocity fields of the 1000-km and 2000-km (both N_L, S_L) wave solutions with periodic lateral boundaries. The cross sections are shown at $t = 96$ h and $t = 336$ h. Contours are shown at intervals of 2 and 5 m s^{-1} for each case, respectively.
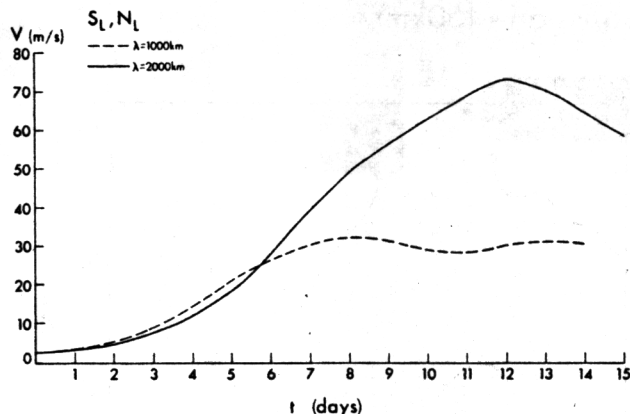
FIG. 8. Profiles showing the time evolution (in days) of the maximum v-velocity (m s^{-1}) for the 1000-km (dashed) and 2000-km (solid) periodic solutions.

baroclinic waves in an Eady flow is the increase in static stability with time by the vertical heat transport associated with the waves. This increased static stability can increase the Rossby radius of deformation, L_R, thereby increasing the scale of the short-wavelength cutoff. The static stability that corresponds to the thermal wind balance, as previously discussed, is of O(Ro) compared to the mean static stability. In the quasigeostrophic framework it is probably negligible to significantly change L_R; perhaps for nongeostrophic regimes this mechanism may be effective. However, one should note that in Gall (1976a) a rather coarse GCM was used for the study, thus limiting the possibility for the baroclinic waves to develop strong frontogenetical regions that could significantly alter their energetics. Our solution tends to display a strong cascade to shorter and shorter scales in the zonal direction; however, the shorter scales are not baroclinic Eady waves as suggested in Drazin's study but rather are characteristic of fronts. It may well be that these processes stabilize the primary baroclinic unstable wave. Horizontal diffusion might be considered as another reason for dissipating short waves faster than long waves. However, Fig. 7 indicates that long waves produce very sharp fronts with scales much smaller than the 1000 km wave; hence, we can conclude that, if dissipation would have stopped the growth of the 1000-km wave, the long wave (2000 km) would not have generated scales shorter than 1000 km. It seems obvious then that the mechanism of cascading to smaller scales and the generation of fronts are primary mechanisms responsible for the leveling off of the baroclinic waves; at the same time, certainly, energy dissipation by diffusive processes may act on the frontal scale. However, as pointed out in Orlanski et al. (1985), ageostrophic effects due to inertial wave dispersion may also act to neutralize frontogenetical processes in the small scale. In a later section we will show the terms of the heat balance equation, and these results will become more apparent.

4. Nonperiodic baroclinic stability

In the previous section we confirmed the fact that short-wave baroclinic instability could develop in shallow layers with low static stability. However, our primary goal is to investigate the stability of localized areas with low static stability in order to explain the occurrence of meso-α cyclones due to the release of surface sensible heat. For that purpose the model described in section 2b will be used with open boundary conditions. At the inflow boundary we prescribe the shear flow and stratification shown in Fig. 3. Superimposed on that flow is a wave structure similar to the periodic case. This permits us to evaluate the difference in evolution of this continuous spectrum in the downstream which is now possible because there are now no constraints on the single horizontal scale, L (other than the limiting scales of the domain size and the grid size). We will briefly mention some of the results from those solutions, but our main emphasis is to discuss the evolution of solitary disturbances such as Gaussian distributions in the horizontal plane. These disturbances are introduced on the left side of the channel and become unstable as they move downstream. This approach also allows us to include the effects of sensible heat release at the boundary in a localized region downstream of the disturbance. Since we now wish to resolve the effects of sensible heat at the lower boundary, we also have increased the vertical resolution from 1000 m to about 300 m. Since the disturbance itself will grow downstream both temporally and spatially, we have fixed the channel length to be 4000 km with $\Delta x = 25$ km.

a. Downstream instability

The evolution of an isolated Gaussian disturbance that initially has a length scale L of 450 km and

$$V = V_0 \cos\left(\frac{\pi}{H}z\right)e^{-(X/L)^2}, \qquad (4.1)$$

can be seen in Fig. 9. The time evolution is shown for 100, 125 and 150 h. The v-velocity as a function of x and z is shown on the right side; corresponding cross sections of perturbation potential temperature are shown on the left. This case does not include surface heating; the vertical profiles correspond to the high stratification, high shear profiles ($N_H S_H$) of Fig. 3. We can see the evolution of the disturbance propagating and growing downstream as predicted. The deviation potential temperature contours show a corresponding baroclinic structure in the lower levels.

The detailed structure of the other variables for this baroclinic wave at 150 h can be seen in Fig. 10, with the potential temperature anomaly and the perturbation u-velocity shown in the upper half and the v and w velocities shown in the lower half. It seems obvious from these results that this meso-baroclinic wave is very shallow. The penetration of the wave will depend on
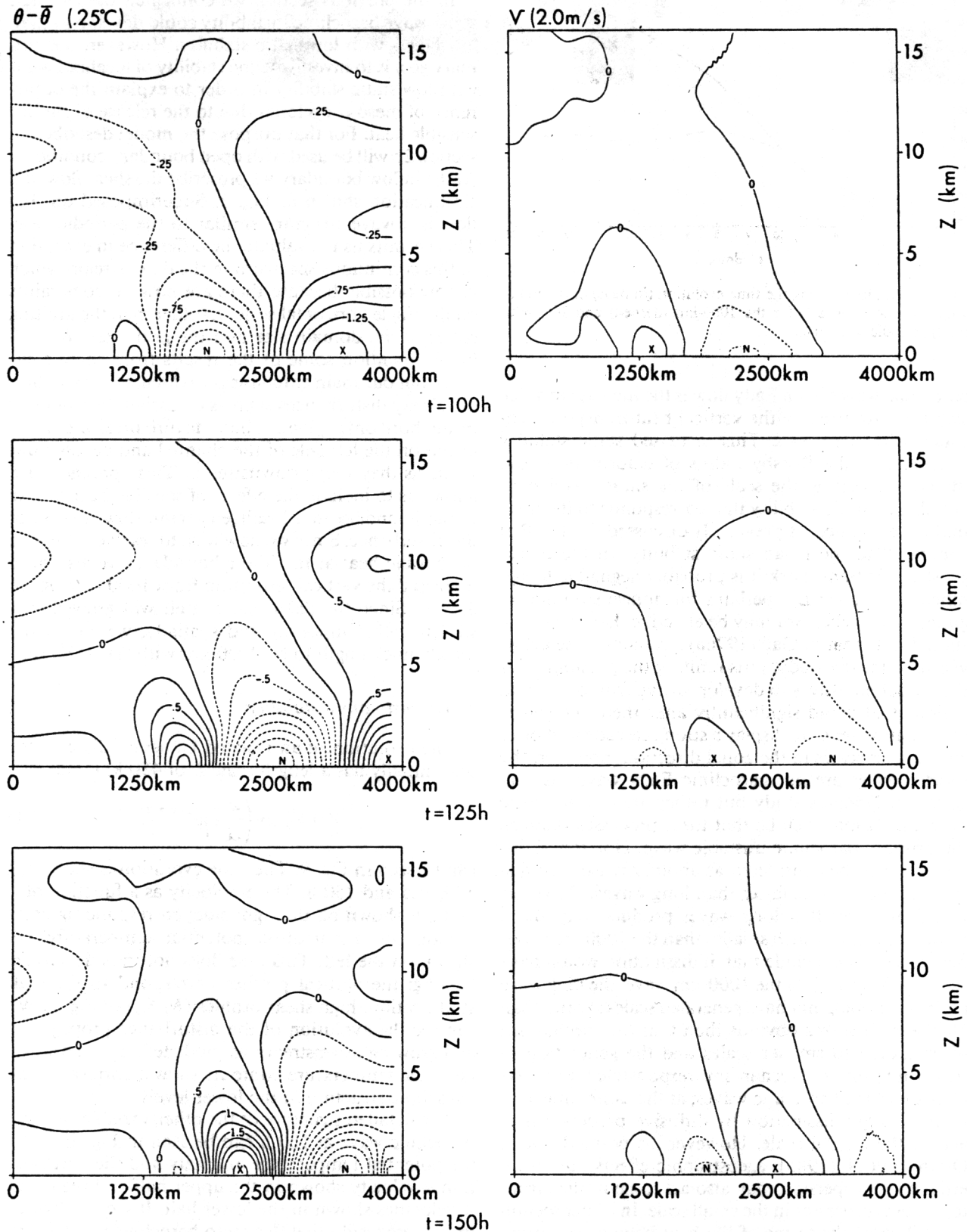
N_H, S_H (open) Init: Gaussian (450km)

FIG. 9. Cross sections showing the time evolution ($t = 100$, 125 and 150 h) of the perturbation potential temperature (left) and v-velocity (right) for a case (N_H, S_H) with lateral open boundaries and an isolated Gaussian initial disturbance (450 km). Contour intervals are 0.25°C and 2 m s^{-1}.

the environmental shear and stratification [as indicated by Eq. (2.12)]. The effects of low shear can be seen in Fig. 11 (for N_H and $t = 200$ h). The upper cross section shows v-velocity for low shear, S_L, and the lower cross section shows the solution for the high shear case, S_H. The amplitude of the high shear case (S_H) is 12 m s^{-1} or roughly four times that of the low shear case (S_L) of 3.5 m s^{-1}. This solution can provide us with a check of the penetration depth, (2.12), for the baroclinically unstable waves, if we assume that δ represents the height at which the amplitude $V(\delta)$ is half the amplitude of V at the surface. The estimated C_r (the propagation velocity) is, for the low shear case,

$$C_r \approx 4.4 \text{ m s}^{-1},$$

and for the high shear case,

$$C_r \approx 7.2 \text{ m s}^{-1}.$$

Since the shear of the S_L case is about half that of the S_H case and since u at the ground is very small compared with C_r, it appears that

$$2\delta \approx \frac{C_r}{du/dz}$$

should not be too different in both cases. In Fig. 11 the v-velocity, equal to half the maximum velocity, is de-

N_H, S_H (open)   Init: Gaussian   (450km)
no surface heat
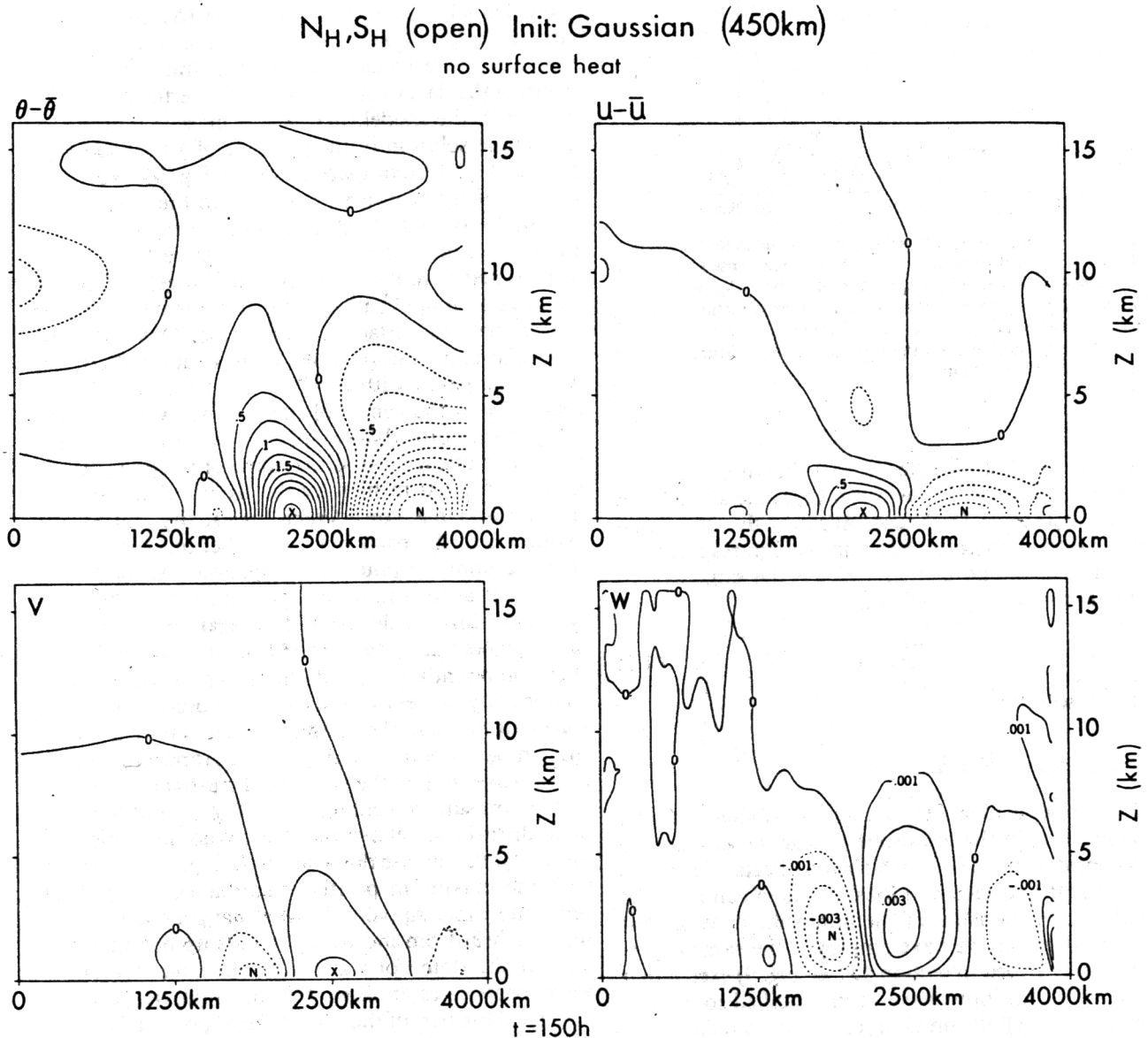
FIG. 10. Cross sections of the perturbation potential temperature, perturbation u-velocity, v- and w-velocities at $t = 150$ h for the N_H, S_H solution with lateral open boundaries and an initial isolated Gaussian disturbance (450 km). Contour intervals are 0.25°C, 0.25, 2.0 and 0.001 m s^{-1} respectively.
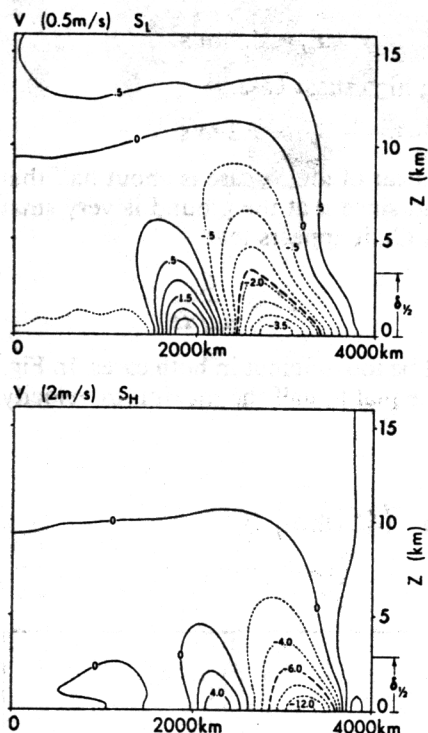
FIG. 11. A comparison of v-velocity cross sections for the 450-km isolated Gaussian disturbance at $t = 200$ h. The cross sections are shown under low shear (S_L, upper) and high shear (S_H, lower) conditions. The heavy dashed contour in each cross section indicates where the v-velocity is equal to half of the maximum velocity. The corresponding δ is shown on the right side of each figure. Contour intervals are 0.5 and 2.0 m s^{-1}.

noted by the dash–dot line with δ shown on the side. The δ is 3.4 km for the low shear (S_L) case and 2.9 km for the high shear (S_H) case. Accordingly, horizontal scales for these cases are 925 and 800 km respectively. The ratio of the horizontal scales is the same as that of the δ, confirming the fact that

$$\frac{N\delta}{fL} \approx 1 \qquad (4.2)$$

for each solution.

b. Localized surface heating

In order to evaluate the stability characteristics of a shallow layer in the atmosphere near the ground, we will consider the case in which the effects of sensible heat near the surface in a localized area can alter the stability characteristics of the atmosphere. With that purpose in mind, we have employed the same experiment as described in section 4a (see Fig. 9) except that the surface conditions have been modified to include heat fluxes. In all the previous cases the boundary condition for θ was given by

$$\theta_z(x, 0, t) = \bar{\theta}_{z_i}(0, 0), \quad \text{for} \quad 0 \leqslant x \leqslant 4000 \text{ km}, \quad (4.3)$$

which implies that the lapse rates at the ground equal the initial lapse rate of the mean profile; in other words, the deviation from the mean profile has a lapse rate of zero. This former condition therefore implied that the lapse rate was constant at the surface for the entire length of the channel. In the experiments designated "surface heating", however, we will have a central region in which different heat fluxes will be imposed; the condition (4.3) will be modified as follows:

$$\theta_z(x, 0, t) = \theta_{z_i}(0, 0), \quad x < 1250 \text{ km} \quad \text{and} \quad x > 2500 \text{ km},$$

$$\theta_z(x, 0, t) = 0, \quad 1250 \text{ km} \leqslant x \leqslant 2500 \text{ km}. \quad (4.4)$$

We can interpret this interior zone as an area in which the sensible heat is producing a neutral adiabatic layer. Profiles similar to the earlier initial conditions will be used, namely, a constant lapse rate (N_L or N_H); the condition $\theta_z = 0$ will slowly erode the constant lapse rate to produce a region with weaker stratification. The depth of that layer will depend on the vertical diffusion, κ, used in the model (here $\kappa = 5$ m^2 s^{-1}). The meso-baroclinic solution in the presence of a heat source is seen in Fig. 12 (compare this with Fig. 9). Note that the v-velocity contours are similar to the "no surface heating" case both in structure and in the position of the maximum and minimum. The largest difference, as expected, is in the intensity of the wave; in this case we have 12.6 m s^{-1} after 150 h as compared to 6.0 m s^{-1} in the "no surface heating" case. Obviously the potential temperature shows considerable differences when compared with the "no surface heating" case, especially in the center of the channel where a large temperature disturbance appears. What is interesting about this disturbance is the dome of warm air which is roughly 2500 m high by the length of the surface heating and has considerable variability during the evolution of the baroclinic wave; hence, it is evident that the dome of potential temperature is shallow at 100 h, yet at the same time we can see that the wave is propagating inside the surface heating region. The dome grows during the period from 100 to 150 h, and then the boundary layer dome seems to collapse and a large eddy moves away. Clearly, the oscillation of the warm air dome in the boundary layer is in phase with the temperature disturbance of the propagating baro-clinic wave; notice the negative disturbance at 100 h in the "no surface heating" case (Fig. 9) and the neg-ative disturbance above the shallow dome in Fig. 12. Similarly, the intense dome at 150 h (Fig. 12) correlates with the maximum positive disturbance of Fig. 9 at the same time. Apparently what happens is that the sensible heat from the ground builds up potential en-ergy in the dome of warm air; when the baroclinic wave propagates through this medium, it becomes larger, taking part of the accumulated potential energy and consequently reducing the intensity of the dome in the boundary layer. A more detailed examination of this phenomenon will be explored when the heat
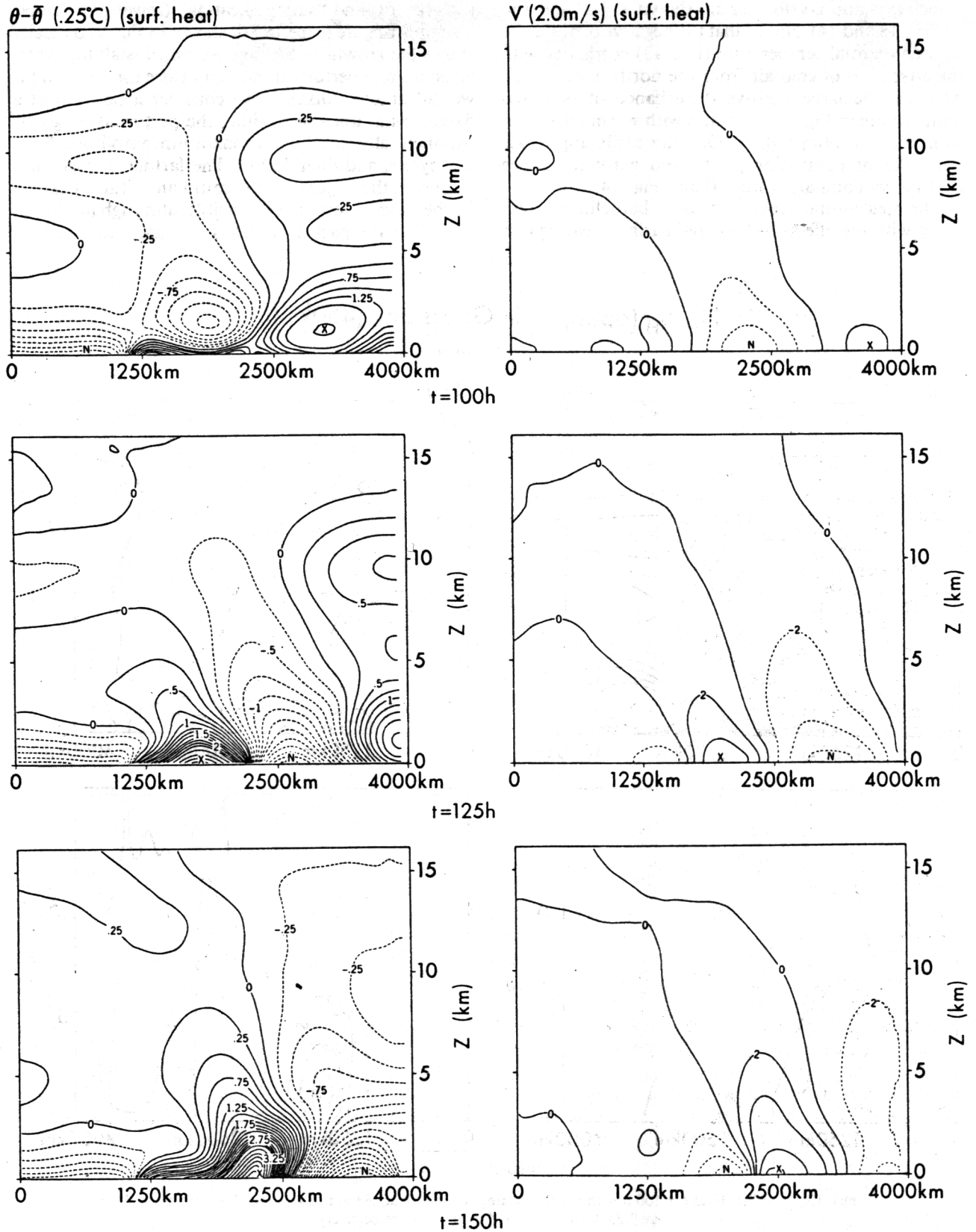
N_H, S_H (open) Init: Gaussian (450km)

$\theta - \bar\theta$ (.25°C) (surf. heat)   V (2.0m/s) (surf. heat)

t=100h

t=125h

t=150h

FIG. 12. As in Fig. 9 except that surface heating ($H_{SFC} > 0$) has been added to this solution. Cross sections are shown at t = 100, 125 and 150 h with contour intervals of 0.25°C and 2.0 m s^{-1}.

balance is discussed. To enhance the description of the baroclinic waves with surface heating, the structure of the perturbation potential temperature, x-perturbation velocity, y- and z-velocities are shown at 100 and 150 h (Figs. 13 and 14). Notice that the negative disturbance in the potential temperature (Fig. 13) correlates with the advection of cold air from the north (v negative); whereas, the large positive disturbance of potential temperature in Fig. 14 correlates with warm advection from the south (v positive). One can easily appreciate the different circulations, with and without surface heating, by comparing Fig. 10 and Fig. 14.

The space–time growth of these baroclinic waves along with the effects of localized surface heating can be seen in Fig. 15. The v-velocity at the surface is plotted as a function of x and the time of integration (in hours). The solutions shown are for the "no surface heating" (upper part) and "surface heating" (lower part) cases. The upper figure (experiment shown in Fig. 9) basically shows the growth of the downstream instability when given a small perturbation at an upstream position (as we did at $x = 20\Delta x$). If we consider a position at a fixed x as a function of time, the perturbation grows exponentially, reaching a maximum amplitude for a few cycles, and then decays. The farther downstream we move, the larger the maximum amplitude attained by the wave becomes. It is possible, although not tested here, that the packet of waves will grow to a certain
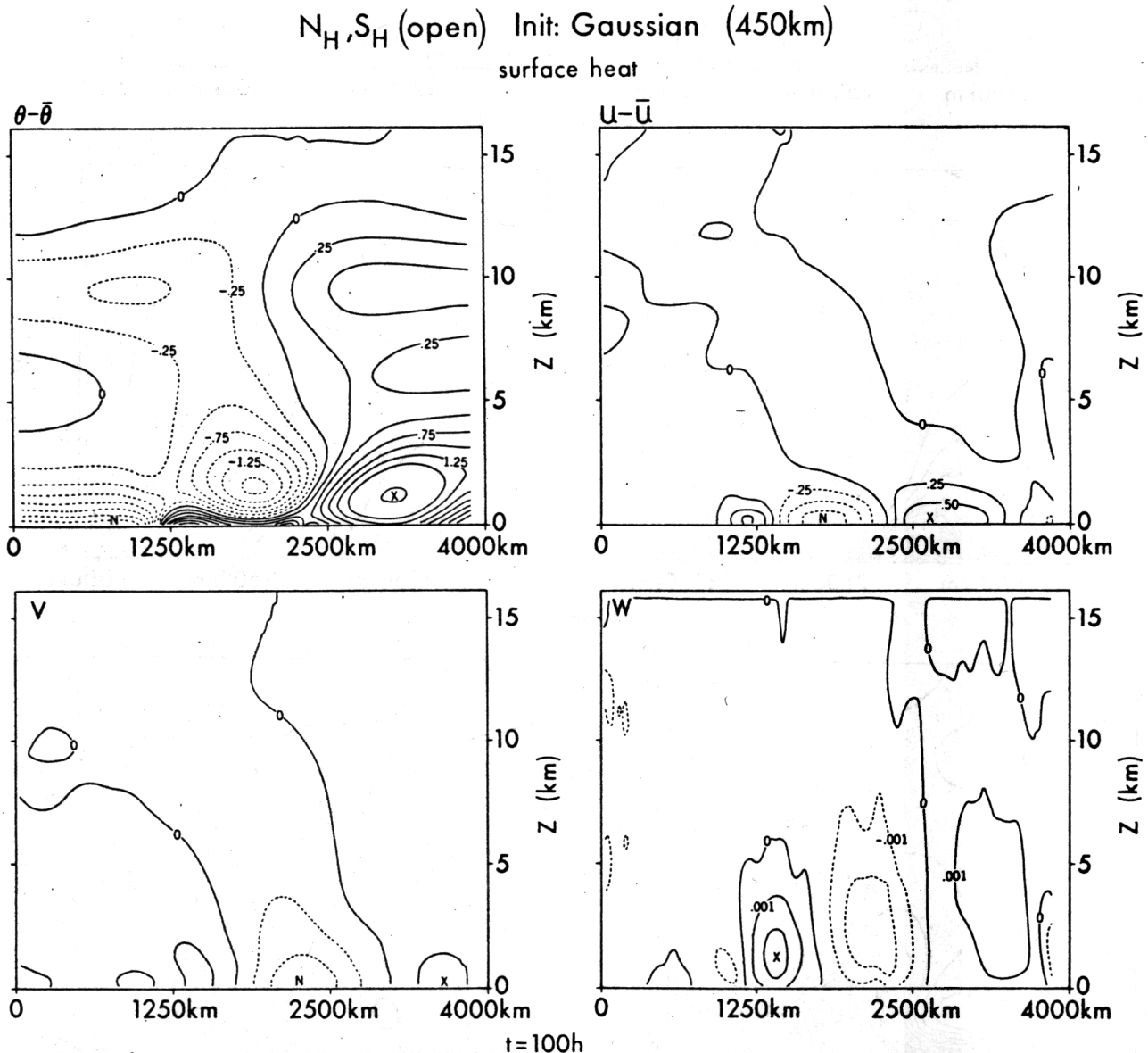

FIG. 13. As in Fig. 10 at $t = 100$ h with surface heating ($H_{SFC} > 0$) added to this solution. Contour intervals are 0.25°C, 0.25, 2.0 and 0.001 m s^{-1} respectively.

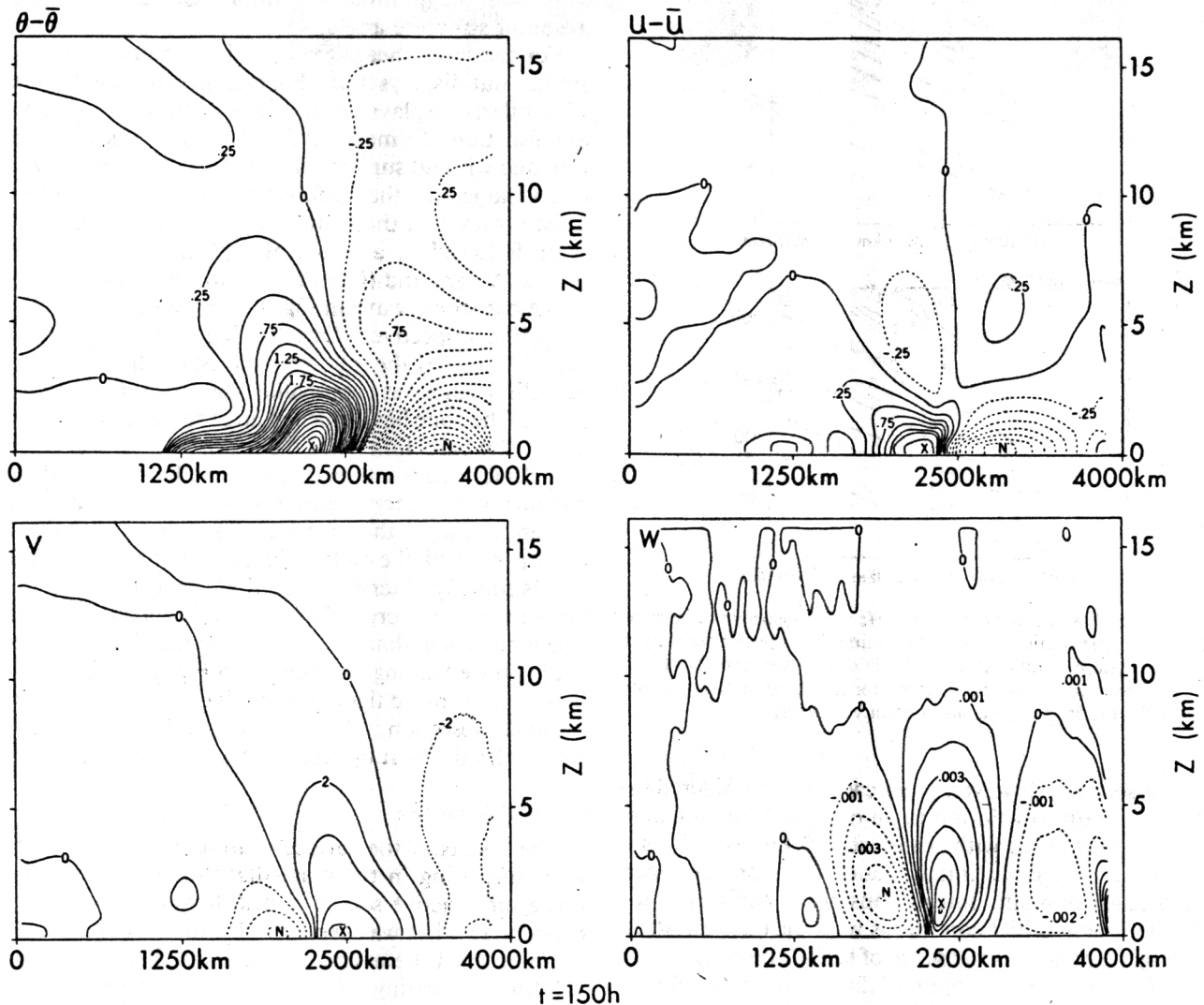## N_H, S_H (open) Init: Gaussian (450km)
surface heat

FIG. 14. As in Fig. 13 but with the cross sections shown at $t = 150$ h. Contour intervals are the same as in Figs. 10 and 13.

amplitude and then remain constant as we observed in the case with finite amplitude periodic waves (Fig. 8).

The lower figure shows a comparable case when surface heating is included. The overall behavior and scale are similar, but the amplitude is about three times larger (minima of -32 m s^{-1} vs -12 m s^{-1}). We notice also that the scale differences are not substantial; however, the estimation of the scale in this figure could be misleading, since each point on the ordinate represents a period of 50 h; this is quite long compared with the period of the wave, approximately 25 h. To compensate for this, one can measure the difference between the maximum and minimum. This measurement indicates that the wavelengths are slightly shorter in the surface heating case. This becomes more apparent from a

comparison of Figs. 10 and 14 which shows the maximum velocity area of the "no surface heating" case to be wider than that of the "surface heating" case. Comparing Figs. 10 and 14 (both for $t = 150$ h), we can see that the maximum surface area shows a length difference of about twenty percent; however, we should not expect the difference to be large since the initial disturbance already was chosen to be small for both cases (450 km).

c. Growth dependence on the shape and scale of the initial disturbance

Until now we have limited our discussion to the evolution of periodic disturbances (§2d) and isolated Gaussian disturbances for the open domain of the pre-
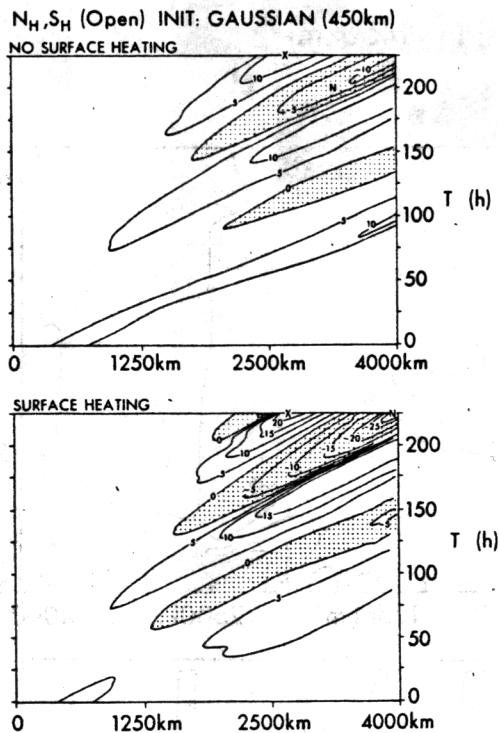
N_H, S_H (Open) INIT: GAUSSIAN (450km)

NO SURFACE HEATING

SURFACE HEATING

FIG. 15. Cross sections of the surface ($z = 0$) v-velocity as a function of x and time of integration, T (in hours). The upper cross section has no surface heating ($H_{SFC} = 0$) while the lower one does ($H_{SFC} > 0$). The contour interval is 5 m s^{-1} for each cross section with the shaded areas denoting regions of negative velocity.

vious section. However, other cases also considered include the time evolution in an open domain of Gaussian disturbances with scales of 700 km as well as a 1000-km wave as initial conditions for the open boundary domain. Integrations were performed for each of these initial conditions with the only variation being the presence or absence of surface heating. Figure 16 shows the time variation of the maximum v-velocity at the surface for each of these cases. As a comparison the time evolution of a 1000-km periodic wave (indicated as "Periodic") is also shown.

The difference in the evolution between the (Periodic) and (Open) cases for the 1000-km wave without surface heating deserves some attention. It appears that the growth rate for the first four days is far larger in the open case than in the periodic case. It is possible that the absence of periodicity in the (Open) case allows for the continuous spectrum to grow much faster than the discrete spectrum of the (Periodic) case (Farrell, 1982). If we compare the former case to the same case with surface heating ($H_{SFC} > 0$), we see that the intensity is basically the same for the first 4–5 days; however, after this period in which the boundary layer grows and releases potential energy to the waves, the solution shows a considerable increase in the growth rate. For that matter, in all the cases where surface heating was present, the growth rate is larger. Also, notice the sim-

ilarity between the evolution of the Gaussian 700 and 450 km disturbances. The labeling scale of the 700 and 450 km curves only refers to the initial conditions, because after the nonlinear evolution, both cases develop a similar structure and scale.

For the large shear case, S_H, the time evolution is similar but displays a much larger growth rate. Figure 17 similarly displays the maximum surface v-velocity as a function of time for the Gaussian (450 km) wave with and without surface heating. As before, the growth rate is larger for the surface heating case after a few days; however, it then enters a period of slow growth again followed by a period of explosive growth. The points (A), (B) and (C) in this figure refer to the state of the baroclinic wave in Fig. 12 for times of 100, 125 and 150 h, respectively. One can characterize the period from (A)–(C) by the following stages: (A) the localized baroclinic zone was very shallow (see upper part of Fig. 12), (B) the zone has deepened and the wave has grown due to the baroclinicity of the mean flow, and (C) the baroclinic zone is interacting with the baroclinic eddy, enhancing the energy transfer to the waves. It has been suggested that, if the upstream boundary is continuously perturbed, the cycle will repeat itself with a period that is roughly determined by the propagation time it takes the wave to cross the localized baroclinic region. The tendency of that pulsation is apparent in the curve with surface heating. Judging from Fig. 17, it does not appear to be more than perhaps two cycles. In fact, in the next subsection it will become more apparent when we discuss the heat budget for these cases.

d. Heat balance

The results of the surface heating case were somewhat surprising in the sense that the boundary layer was a more active source of heat fluxes to the disturbance than what was expected. In this section we will examine the time average of the heat fluxes for both the "surface heating" ($H_{SFC} > 0$) and "no surface heating" ($H_{SFC} = 0$) cases. Basically the potential temperature equation of (2.4) can be averaged for a period of time of 500 time steps or 25 h. The average heat advection terms contributing to this equation are given as follows:

$$\left\langle \frac{\Delta\theta}{\Delta t} \right\rangle = \langle -v\theta_y \rangle + \langle -u\theta_x \rangle + \langle -w\theta_z \rangle + \langle \text{diff}\theta \rangle, \quad (4.5)$$

where the notation, $\langle f \rangle$, represents the time average of f and Δt is the time step. The first term $\langle -v\theta_y \rangle$ is the value of the meridional heat advection, the primary source of baroclinic instability; $\langle -u\theta_x \rangle$ and $\langle -w\theta_z \rangle$ are the values of the horizontal and vertical heat advection in the cross-stream circulation associated with the baroclinic wave. The $\langle \text{diff}\theta \rangle$ represents the diffusive effects operating in the model. Figure 18 shows the contribution of each term (in units of 10^{-4} °C s^{-1}) for the "$H_{SFC} = 0$" case (Fig. 9) at $t = 100$ h. We can see that, although the large terms are $\langle -u\theta_x \rangle$ and $\langle -w\theta_z \rangle$,
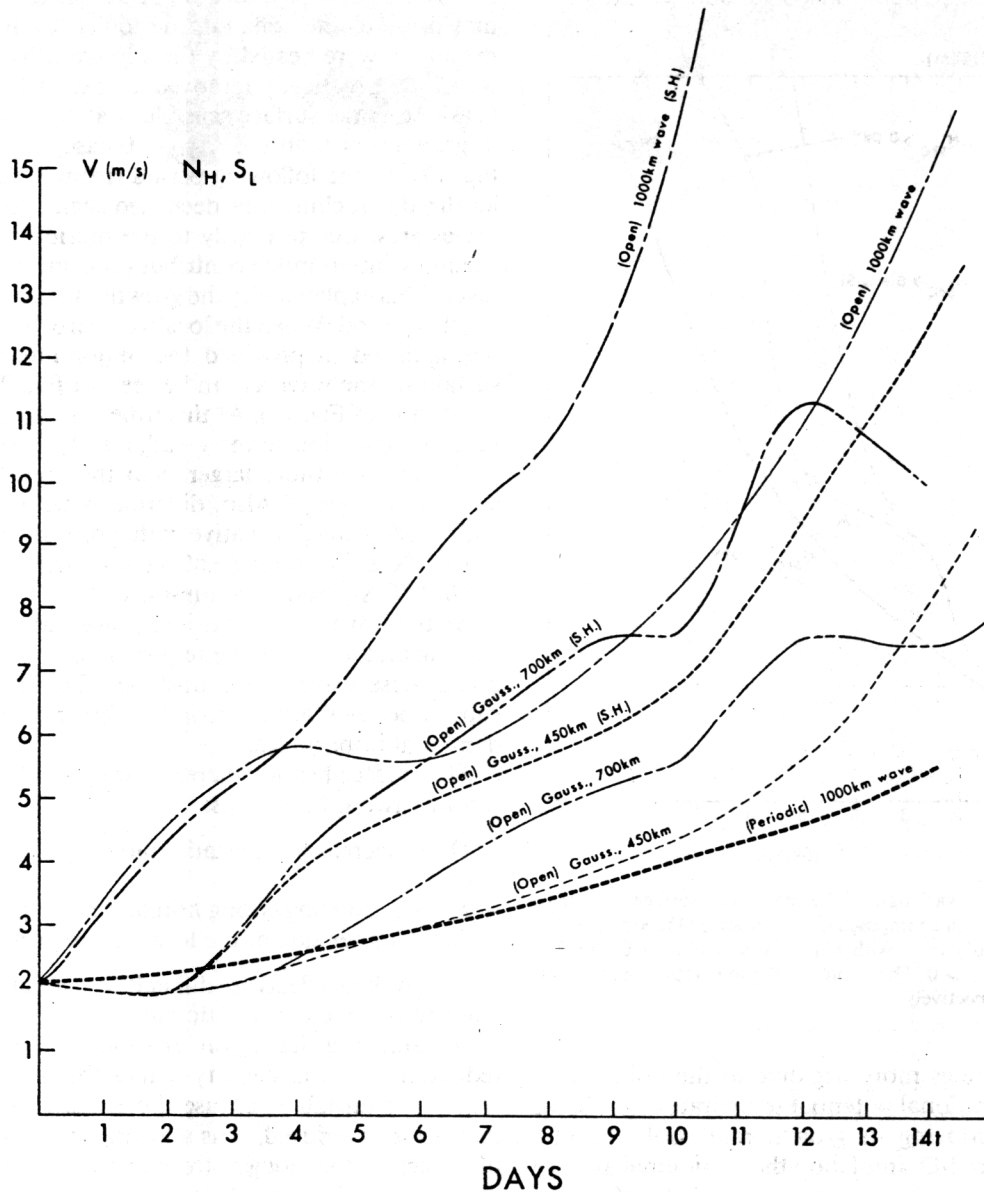
FIG. 16. The time variation of the maximum surface v-velocity for the N_H, S_L solutions with open lateral boundaries. Each case has an imposed isolated Gaussian disturbance of 1000, 700 or 450 km and each of those are shown with $H_{SFC} = 0$ and $H_{SFC} > 0$. The maximum v-velocity of a periodic case with an imposed wave of 1000 km is shown for comparison.

they seem to be out of phase and cancel each other. Thus, it appears that $\langle -v\theta_y \rangle$ provides the largest change of potential temperature. The meridional heat flux $\langle v\theta \rangle$ at the surface will be positive for baroclinically unstable waves; it will tend to destroy the temperature gradient and flatten the isentropes at the surface. This effect can be seen indirectly by the large contribution of positive meridional heat advection shown as negative for $\langle -v\theta_y \rangle$ in the upper left cross section of Fig. 18. The gradient $\theta_y = \theta_{gy}$ is constant for the entire model integration and since θ_{gy} is negative for the colder poleward gradients to the north; therefore, the term $\langle -v\theta_y \rangle$

$= -\theta_{gy}\langle v \rangle$ is proportional to the average of the meridional velocity $\langle v \rangle$ and thus, negative or positive values of $\langle -v\theta_y \rangle$ will imply negative or positive values of $\langle v \rangle$. Inspection of the contribution of the diffusive term shown in the graph on the lower left of Fig. 18 shows it to be negligible. Obviously the difference of these four terms will be the change in the net potential temperature during this time interval; in fact, one can see the negative temperature anomaly in Fig. 9. This negative value is correlated positively with $\langle v \rangle$, implying a positive meridional heat flux. Basically, the wave continues to grow as the meridional (negative) heat
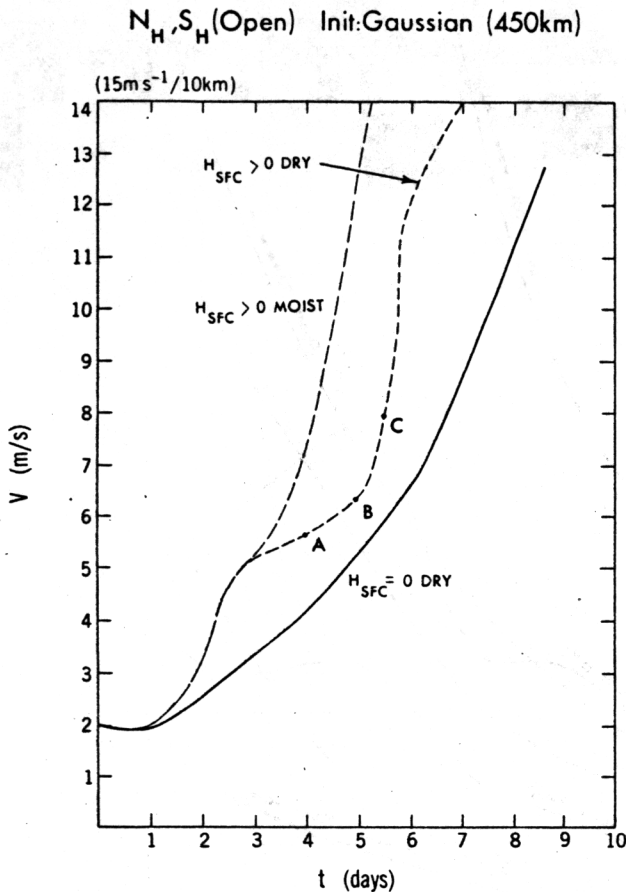
N_H, S_H (Open) Init:Gaussian (450km)

FIG. 17. The time variation of the maximum surface v-velocity for the N_H, S_H case with an imposed Gaussian wave (450 km). Profiles are shown for the dry cases with $H_{SFC} = 0$ and $H_{SFC} > 0$, and the moist case with $H_{SFC} > 0$. The points A, B and C represent $t = 100$, 125 and 150 h, respectively.

advection becomes more negative to the point of reducing the meridional potential temperature gradients and thereby reducing its growth rate (Gall, 1976b). However, in this 2-D simulation the meridional average potential temperature cannot vary and therefore becomes a constant source of potential energy.

The evolution of the baroclinic instability with localized surface heating as seen previously (§4b and Figs. 12–14) gives a new dimension to the evolution of those waves and deserves special attention. In Fig. 19 we show the heat budget of the $H_{SFC} > 0$ case for the wave evolution at 100 h (see Fig. 13); this time also corresponds to point (A) of Fig. 17. Immediately, one can see that the meridional heat advection is structurally similar but 50 percent more intense than the previous $H_{SFC} = 0$ case, with the excess essentially being compensated by the positive heat contribution from the diffusive terms (lower cross section of Fig. 19). Accordingly, the horizontal and vertical heat advection of the cross-stream circulation are proportionally more intense as well. One should emphasize that this period of time corresponds to the time soon after the localized

heat source collapsed; examination of Fig. 13 indicates that prior to the collapse, the lower levels of the atmosphere were heated by the surface fluxes, until the wave had practically removed all excess heating. The heat due to the surface sensible heat caused the waves to grow faster than the $H_{SFC} = 0$ case (see point A of Fig. 17). In the following period (from A to B), as the localized baroclinic zone deepened again, the baroclinic waves grew due primarily to the meridional heat advection without much contribution from the boundary layer. This explains why the growth rate decreased during this period. When the localized baroclinic zone was reestablished, it provided the major mechanism for sustaining the wave as can be seen in Fig. 20 ($t = 150$ h, point C of Fig. 17). At this time, the horizontal and vertical advection terms $\langle -u\theta_x \rangle$ and $\langle -w\theta_z \rangle$ respectively, are five times larger than the meridional heat advection, $\langle -v\theta_y \rangle$. Also, differences between $\langle -u\theta_x \rangle$ and $\langle -w\theta_z \rangle$ are all negative with a minimum of -0.31×10^{-4} °C s^{-1} whereas $\langle -v\theta_y \rangle$ has a maximum of 1.49 $\times 10^{-4}$ °C s^{-1} and a minimum of -0.975×10^{-4} °C s^{-1} in the wave. Therefore, it appears that the localized heating area provides the required potential energy to make these waves more unstable. This contribution cannot be regarded as secondary but rather is of fundamental importance.

The surface heating increases the local baroclinicity through two mechanisms:

1) by decreasing the static stability of the heated region;
2) by producing strong horizontal temperature gradients at either side of the localized region.

Although these effects are difficult to separate, it is most likely that the reduced static stability is the major effect in destabilizing the region. It should be noted that a reduction in static stability makes the baroclinic flow (θ_{gy}) more unstable because the Rossby radius of deformation is reduced, thus allowing more waves to be unstable; in the nongeostrophic regime, this growth rate increase is inversely proportional to the stratification.

5. Moist environment

a. Overview

The importance of latent heat release in meso-convective storms is well recognized. Once a storm is organized on some scale, the moist fluxes from the surface layer will generate latent heat when the level of condensation is reached and will greatly enhance the mesoscale circulation (Orlanski et al., 1985). However, the early concepts of CISK mechanisms may not actually be appropriate for parameterizing latent heat release in meso-convective storms, since it has been shown that moist dynamics in mesoscale processes may considerably change the environment in which those
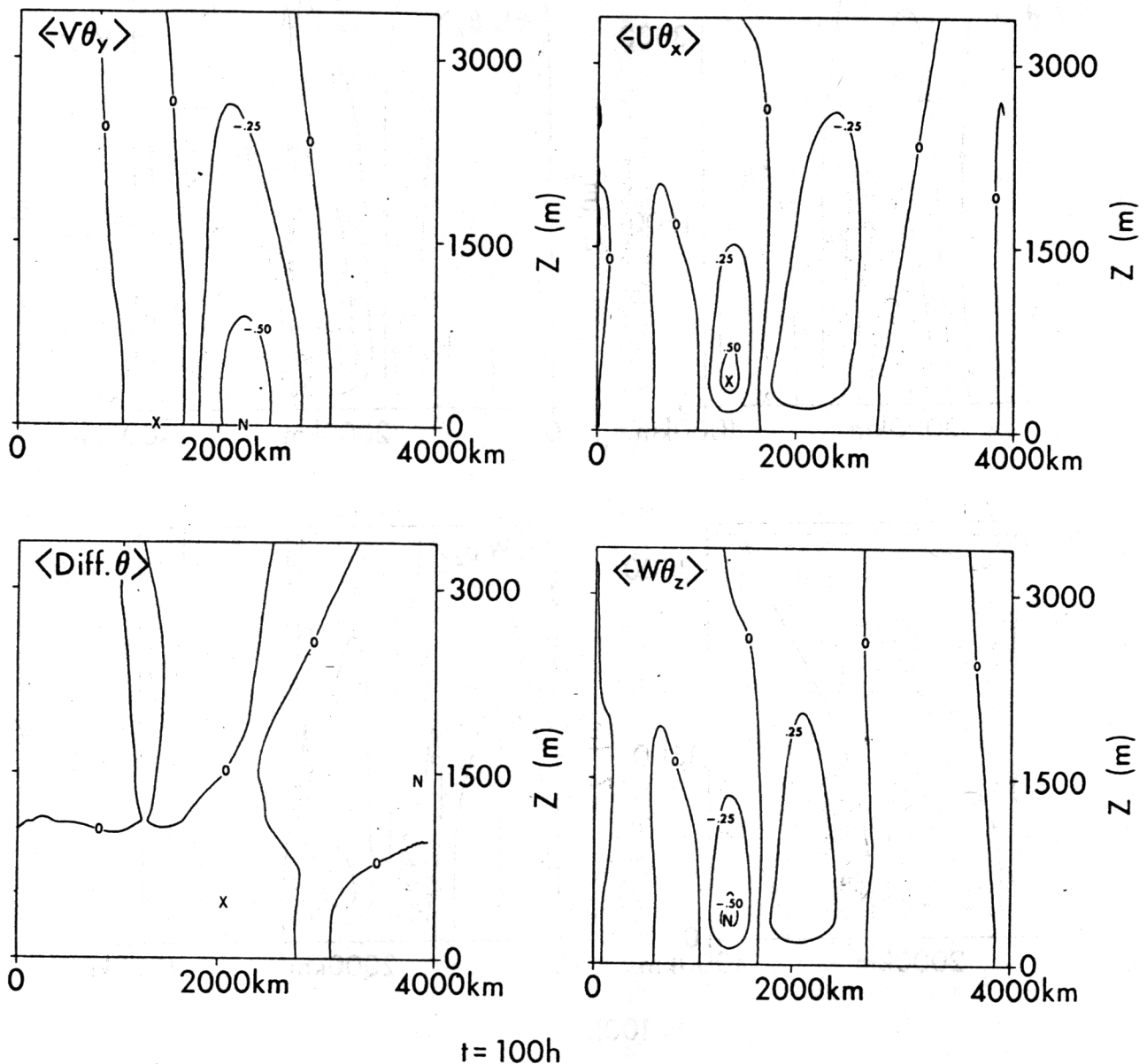
HEAT BALANCE ($°C \ s^{-1} \times 10^4$)

N_H, S_H (Open) Init: Gaussian (450km)

FIG. 18. Cross sections of the time averaged heat advections (in units of 10^{-4} °C s^{-1}), meridional $\langle -v\theta_y \rangle$, horizontal $\langle -u\theta_x \rangle$, vertical $\langle -w\theta_z \rangle$, and diffusion $\langle \text{diff}\theta \rangle$ for the imposed 450 km Gaussian wave at t = 100 h. Contour intervals are 0.25 $\times$ 10^{-4} °C s^{-1} for each cross section.

disturbances are developed. It has been pointed out (Orlanski et al., 1985) that, in the simulations of atmospheric fronts, the effects of moisture not only can generate frontal convective bands but also can drastically modify the frontal circulation. The study concluded that the surface dynamics of moist and dry fronts are similar; however, moist fronts are considerably deeper than dry fronts due to the latent heat release and the apparent reduction in moist static stability of the atmosphere. In fact, an examination of such simulations reveals that the circulation in fronts of a dry atmosphere follows isentropic surfaces (con-
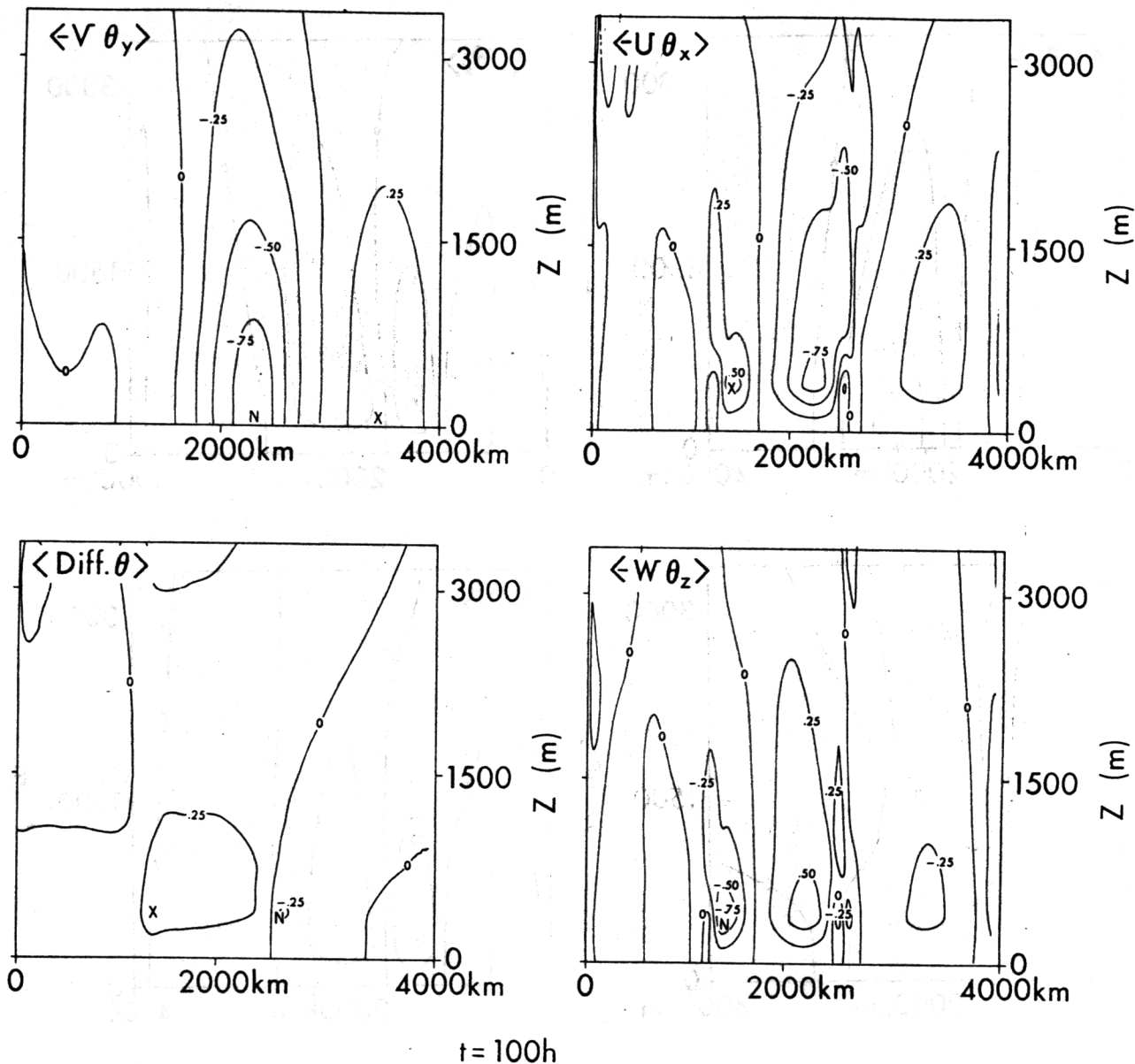
HEAT BALANCE (°C s^{-1} x 10^4)

(Surf. heat) N$_H$, S$_H$ (Open) Init: Gaussian (450km)

t = 100h

FIG. 19. Cross sections shown for $t = 100$ h as in Fig. 18 except that $H_{SFC} > 0$ in this case. The contour interval is 0.25×10^{-4} °C s^{-1} for each cross section.

servation of potential temperature), whereas the circulation in fronts of moist environments follows surfaces of constant equivalent potential temperature. This explains the much steeper and deeper nature of the moist case. In this section we will investigate the effects of moisture and latent heat release on the meso-baroclinic waves which were discussed in the previous sec-

tions. The details of the moist numerical model are described in the Appendix.

b. The moist solution

Aside from the addition of moisture, the solutions were integrated using the same initial and mean flow conditions as the surface heating cases of the previous
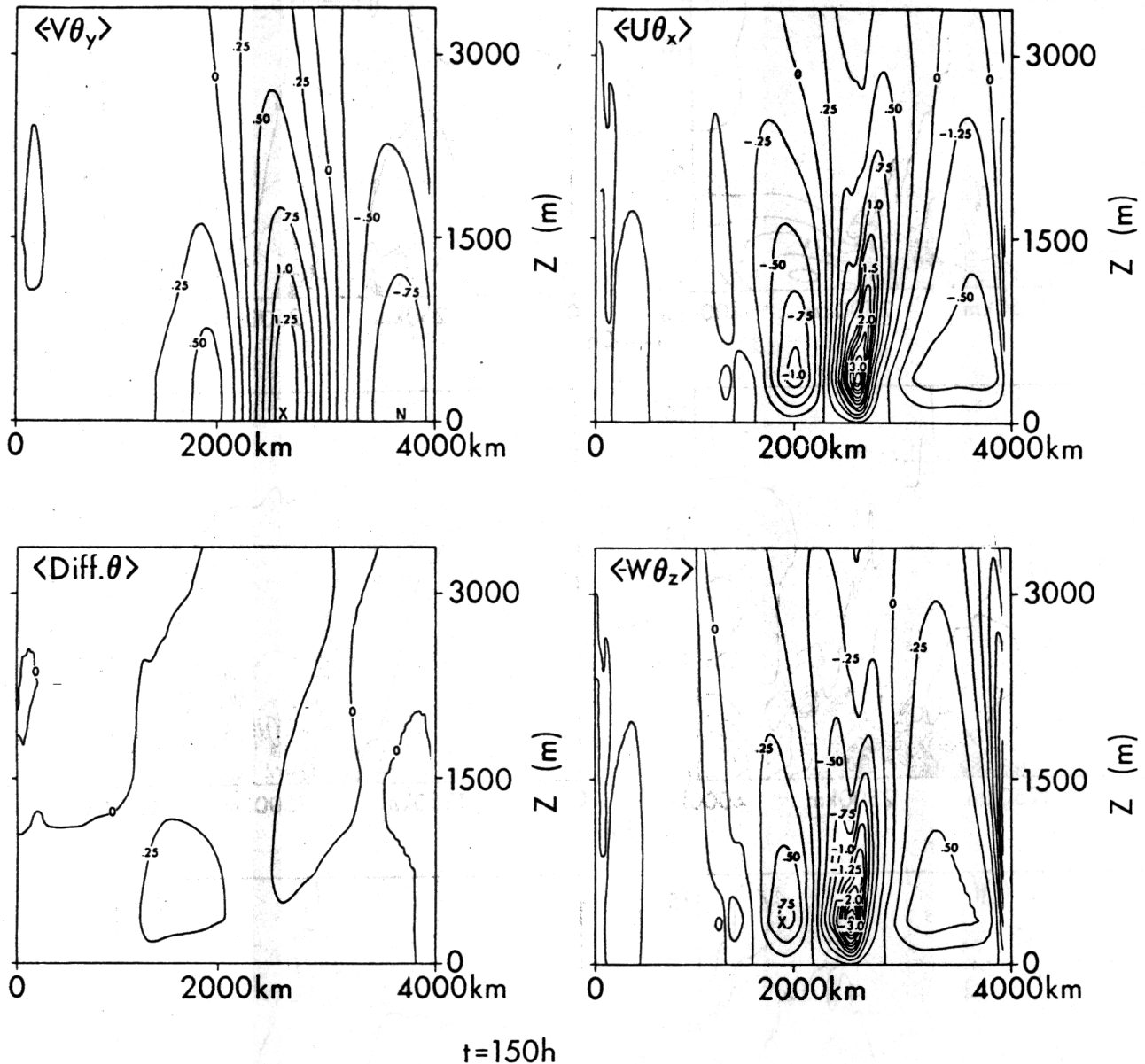
HEAT BALANCE $(°C \ s^{-1} \times 10^4)$

N_H, S_H (Open)   Init: Gaussian (450km)

t=150h

FIG. 20. Cross sections shown at $t = 150$ h for the case shown in Fig. 19. The contour interval is 0.25×10^{-4} °C s^{-1}.

sections. Let us first consider the solution for N_H, S_H where Fig. 21 shows the potential temperature distribution and v-velocity fields at $t = 100, 125$ and 150 h. Note that these solutions are noisier than their counterparts shown in Fig. 12 due to the unfiltered explicit convection scheme used in this model. Then as one would expect, the penetrative convection generates internal gravity waves as we can see from the model so-

lution. The large-scale features at 100 h are similar to those of Fig. 12, but we also notice that the fields are more intense and already have surface velocities which are three times larger than the dry case. Inspecting the potential temperature anomaly (upper left cross section), we notice that the large negative anomaly of Fig. 12 is much more intense, irregular and, in general, shallow. This is due to the fact that convection had
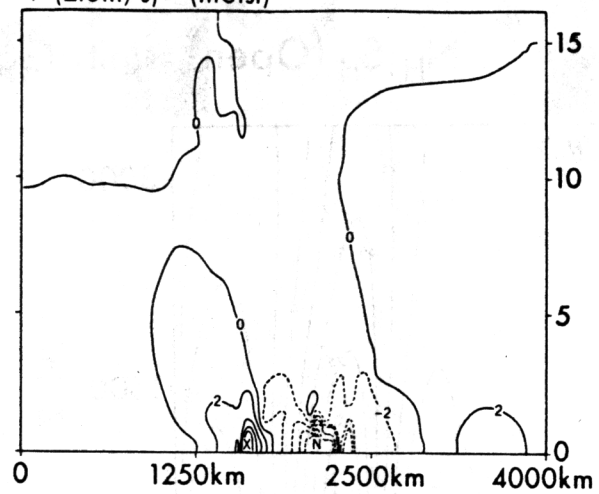
N_H, S_H (open)   Init. Gaussian   (450km)
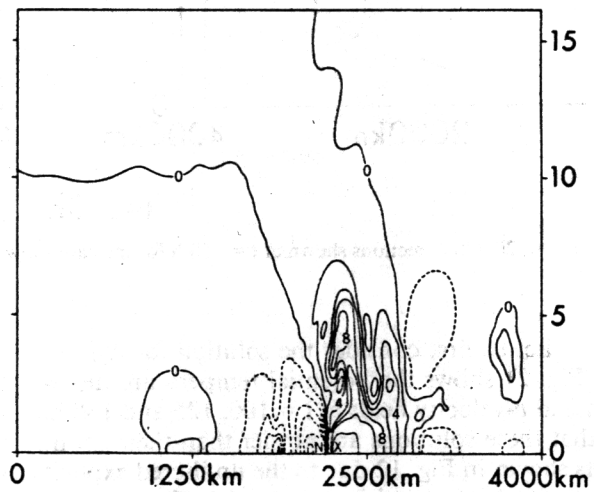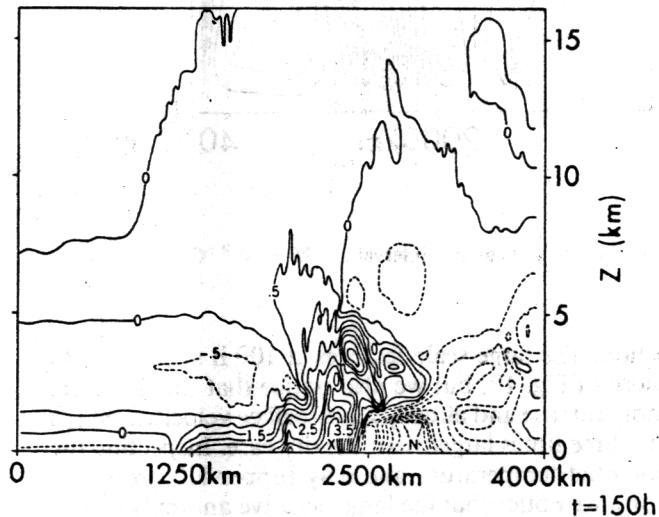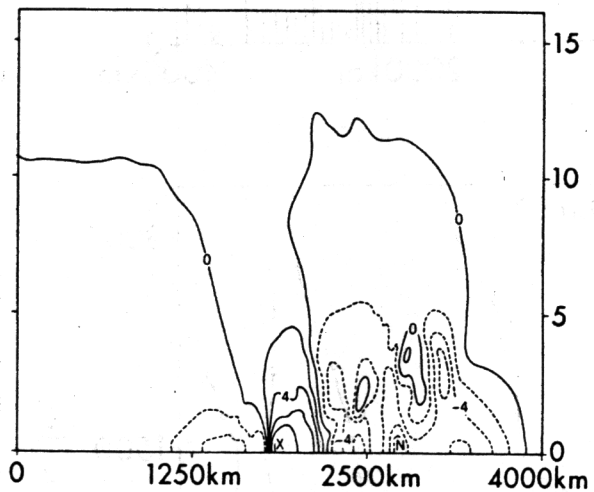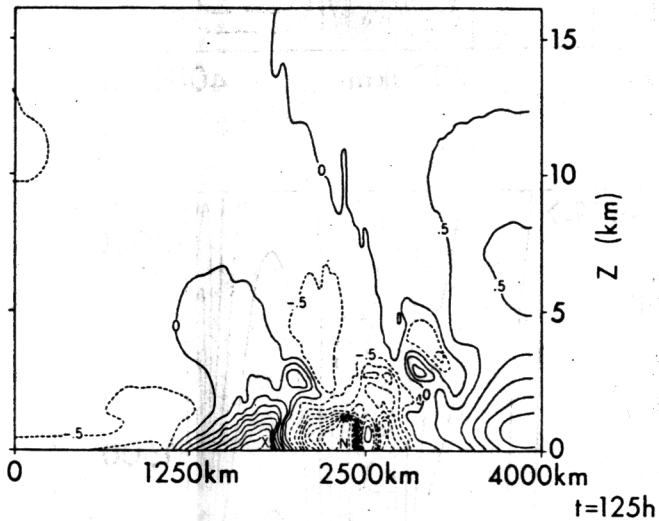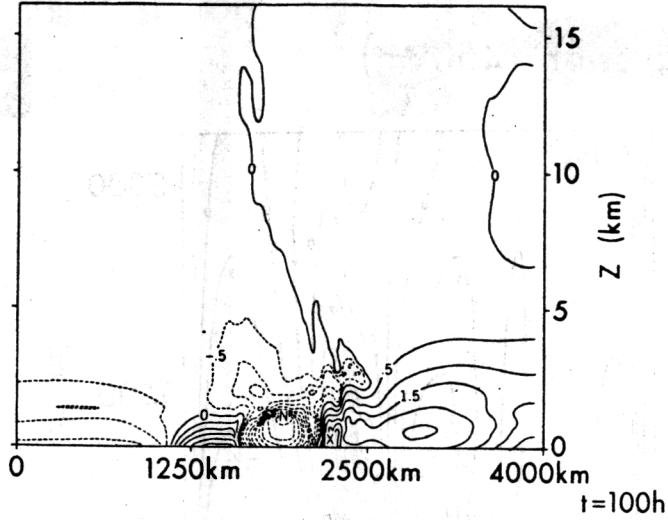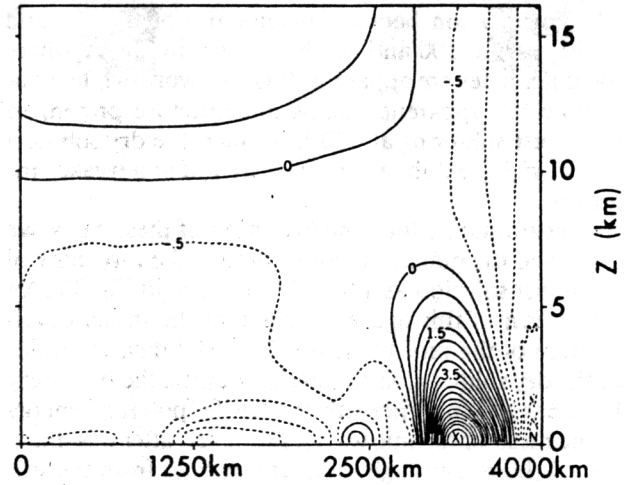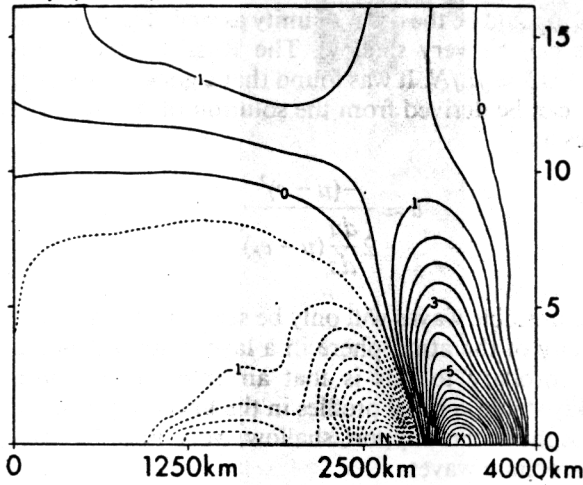

FIG. 21. Cross sections showing the time evolution (100, 125 and 150 h) of the perturbation potential temperature and the v-velocity for the moist version of the solution described in Fig. 12. Contour intervals are 0.5°C and 2.0 m s^{-1}.

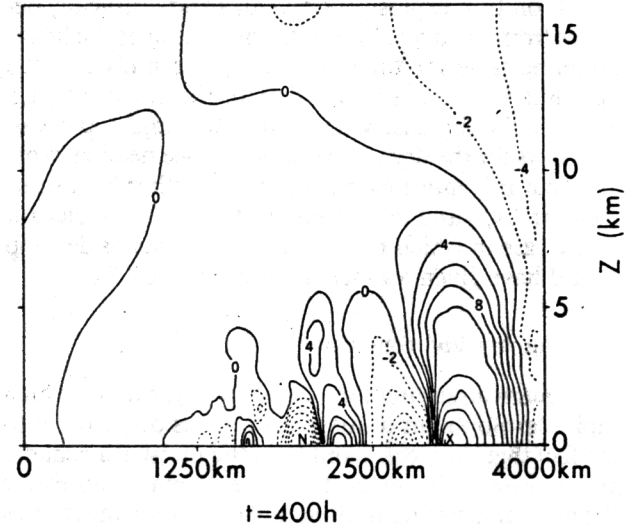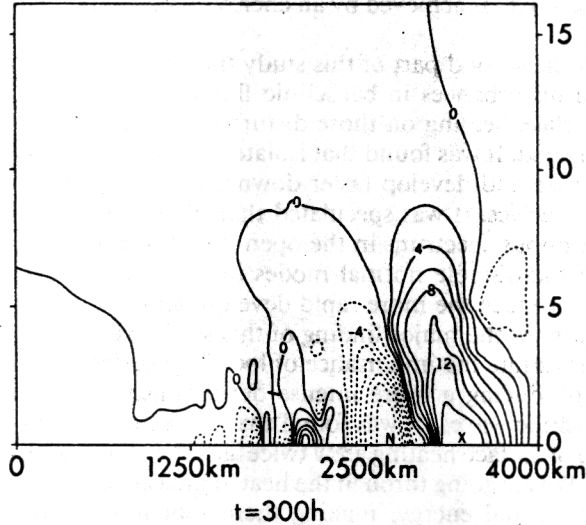## N_H, S_L (open) Init: Gaussian (450km)
V-velocity (surf. heat)

FIG. 22. A comparison of the v-velocity fields at t = 300 and 400 h for the dry and moist solutions (N_H, S_L); initial Gaussian wave of 450 km with surface heating ($H_{SFC} > 0$). Contour intervals are 0.5 m s^{-1} for the dry case and 2.0 m s^{-1} for the moist case.

developed prior to this time and now adiabatic cooling and diffusion in the lower levels are responsible for this stronger negative anomaly. The rather shallow extent here as compared to the dry case is apparently due to latent heat release from the convection. This is certainly more obvious in the subsequent times (125 and 150 h) where the isolated positive maximums can be observed. The v-velocity is also characterized by similar features as in the dry case but is clearly more intensified. For example, at t = 150 h the maximum velocity in the dry case is 8 m s^{-1}, whereas the moist case exhibits a maximum velocity of 17 m s^{-1}. Although moist convection per se somehow clouds the issue of the dynamic evolution of the meso-baroclinic wave due to the natural high-frequency component, it becomes clear that

the considerable increase in the intensity as well as the penetration depth of the storm is much more extended in the latter case. For example, notice that at 150 h the dry solution exhibits only a 0.5°C temperature anomaly fluctuation and 2 m s^{-1} wind disturbance at 5 km (about 500 mb), whereas values of 3°C temperature anomaly and 8 m s^{-1} wind disturbance are clearly evident in the moist case which supports the fact that the storm is more intense and deeper due to latent heat effects.

Another obvious effect of the increased horizontal convergence is the enhanced horizontal gradients of v-velocity (the vertical component of the vorticity). Upon comparing Figs. 12 and 21 we see that the velocity in the moist case increases by a factor of 2, and since the

horizontal scale for the maximum and minimum has been reduced to half that of the dry case, this implies that the vorticity will be 4 times as intense. In the weaker shear flow (S_L) case, the behavior is similar. The comparison between v-velocities of the dry and moist cases at 300 and 400 h is shown in Fig. 22 where the differences are apparent. It is also worthwhile mentioning the apparent small-scale structure present in the moist solutions at 400 h. In fact, the dry solution (upper right) exhibited this feature but at a weaker intensity.

To summarize the time evolution of these cases, we displayed the maximum amplitude of the v-velocity of the moist solution as a function of time in Fig. 17. An inspection of this figure reveals that the initial development of the moist case for the first 3 days is similar to the dry solution; in this period of time the boundary layer has grown sufficiently to transfer potential energy to the meso-baroclinic waves. However, after this initial period there is enough moisture transfer from the surface layers to the environment to make those waves moist convectively unstable. From that point on the moist solution explosively develops and drastically deviates from the dry solution. If one calculates the linear doubling time for these solutions, one finds that the doubling time is less than 1 day for the moist case, 1.5 days for the dry case with surface heating, and about 2.75 days for the dry case with no surface heating. Note also that this moist case employed a rather high stratification (N_H) and that weaker static stabilities relevant to the case in which moist convective systems develop would have given a much shorter time scale.

6. Summary and conclusions

Numerical simulations of winter storms in which rapid development of meso-α cyclones occur point to the fact that the weak stability of the moist atmosphere and release of latent heat are the primary causes for the explosive nature of these storms. The same studies however suggest that instabilities of the dry, prestorm environment can be responsible for the scale selection and position of the storm. In this paper we have discussed mechanisms for baroclinic instability on the mesoscale. The study, using a two-dimensional model to solve the initial value problem describing the evolution of disturbances on a mean baroclinic state, has investigated three main problems:

(i) the effect of static stability on meso-baroclinic waves in a periodic domain (§2d and §3),
(ii) downstream instability in an open domain and the effect of surface sensible heat (§4),
(iii) the effect of moisture on these unstable waves (§5).

Based on the results of Part I we can conclude that a flow can be unstable to support meso-baroclinic waves. The requirement (less than 1000 km wavelength) for these waves to be unstable is similar to that for planetary quasi-geostrophic baroclinic waves. Basically, the particle slope should be less than the isentropic slopes, implying that the Burger number should be of the order of unity. Then, since the Ro $\approx$ 1 for these mesowaves, the Ri should be the order of unity as well. The resulting wave can be very shallow. The Rossby penetration depth is $\delta \approx fL/N$. It was found that a good estimation for δ can be derived from the solution of the unstable waves as

$$\delta \approx \frac{-(u-c)^2}{2\dfrac{du}{dz}(u-c_r)};$$

these unstable waves will only be sensitive to the baroclinicity of the atmosphere in a layer with a depth δ. The corollary to this is that an environment with weakly stable vertical profiles in the lower levels of the atmosphere can support shallow, very unstable meso-baroclinic waves.

The characteristics of the finite amplitude unstable waves suggest that the limiting amplitude for the baroclinic waves is achieved by an energy cascade to *frontal scales.*

In the second part of this study the behavior of isolated disturbances in baroclinic flows and the effects of surface heating on those disturbances has been investigated. It was found that isolated disturbances may organize and develop faster downstream than do periodic waves. It was speculated that the presence of a continuous spectrum in the open domain case rather than the discrete normal modes in the periodic case may produce the more rapid development.

Perhaps the major finding of this study has been to demonstrate the importance of localized surface heating producing a more intense development of short baroclinic waves. It was found that waves in the presence of surface heating grew twice as fast as those without. Waves going through the heated area acquired extra potential energy, making them that much more unstable. Heat flux calculations show that the waves transport as much heat from the north-south temperature gradients (classical baroclinic waves) as from the localized heated region. This result strongly suggests a mechanism for the rapid development of winter storms over ocean surfaces such as coastal cyclones, comma clouds, polar lows, etc. With the passage of a cold front or a land–sea contrast, cold air can be advected over the rather warm ocean surface; the heat fluxes from the ocean will then rapidly reduce the static stability of the atmosphere in the first kilometer, increasing the baroclinicity and thereby allowing meso-baroclinic waves to develop. These waves are shallow, having a depth of the boundary layer and horizontal scales ($L \approx N\delta/f$) of a few hundred kilometers. They can organize convergence of surface moisture in those scales. With this addition of moisture, the wave will explosively develop into an intense meso-α cyclone, which

is in agreement with the results of the last part of the study.

Acknowledgments. I wish to extend my deepest appreciation to Mr. Larry Polinsky for his assistance in the execution of the model integration and analysis. I would also like to thank Dr. Isaac Held for suggestions and comments that improved and clarified this paper, Drs. Bruce Ross and Jerry Mahlman for editorial comments, and Drs. Dan Keyser and Stephen Mudrick for providing a thorough review of the paper. I would also like to thank the GFDL drafting department and Mr. John Conner for their assistance in preparing the figures, and finally, to Ms. Joyce Kennedy for typing the manuscript.

APPENDIX

Model Description

The derivation of the moist equations is similar to that discussed in Ross and Orlanski (1978). A summary of the procedure along with modifications to the previous scheme will be presented here.

The only change in the momentum equations occurs in the buoyancy term of the equation for vorticity (Eq. 2.2). This change, which is underlined in the following equation, results from the positive buoyancy of the water vapor and the negative buoyancy of the liquid water:

$$\frac{\partial \zeta}{\partial t} - J(\psi, \alpha_0 \zeta) = f\frac{\partial v}{\partial z} - g\frac{\partial}{\partial x}\left[\frac{\theta}{\theta_0} + 0.001(0.608q - c)\right]$$
$$+ \frac{\partial}{\partial x}\left(K\nu_e\frac{\partial \zeta}{\partial x}\right) + \frac{\partial}{\partial z}\left(\nu_e\frac{\partial \zeta}{\partial z}\right). \quad \text{(A1)}$$

The variables q and c are water vapor and condensed water mixing ratio respectively in g kg^{-1}. The factor, 0.001, in the buoyancy term is needed to make the mixing ratio dimensionless.

The fundamental change in the present model due to moisture is the inclusion of conservation equations for water vapor and condensed water, and the accompanying source term in the thermodynamic equation for latent heat release. Because of the inability of the model to resolve detailed cloud structure due to the present horizontal resolution, it was felt to be inappropriate to include a rain water or frozen water phase. In the case of rain water, the approach to be taken here is that any condensed water amount in excess of a threshold value of 1.5 g kg^{-1} would be irreversibly removed from the atmosphere. (The procedure of converting condensed water in excess of a prescribed amount to rain droplets was used by Takeda, 1965, and others.)

The primary mechanism of interest in the moisture budget is the treatment of phase changes between vapor and liquid states. We assume in the model that any water vapor in excess of an effective saturation mixing ratio kq_s immediately condenses, where $k \leqslant 1$. The

factor k, which will be set to 0.95 here, is included in the condensation scheme in view of the fact that the mixing ratio q at each grid point is averaged over a 25 km wide box and begins to condense when the average relative humidity over this box is less than 100%, as discussed in Ross and Orlanski (1978).

The method used in computing the water condensed or evaporated in one time step must account for the feedback effect which the temperature change due to latent heat release has upon the saturation mixing ratio, q_s (Asai, 1962). The procedure used here is described below and is similar to the scheme presented by Takeda (1971) and Lipps (1977).

Tentative values of potential temperature, θ', and moisture quantities, q' and c', are obtained for the time $t + \Delta t$ with the assumption that no condensation or evaporation takes place. Thus with leapfrog time differencing, the equations may be written

$$\theta'(t + \Delta t) = \theta(t - \Delta t) + 2\Delta t\left[\alpha_0 J(\psi, \theta) - v\frac{\partial \theta_g}{\partial y}\right.$$
$$\left. + \frac{\partial}{\partial x}\left(K\kappa_e\frac{\partial \theta}{\partial x}\right) + \frac{\partial}{\partial z}\left(\kappa_e\frac{\partial \theta}{\partial z}\right)\right], \quad \text{(A2)}$$

$$q'(t + \Delta t) = q(t - \Delta t)$$
$$+ 2\Delta t\left[\alpha_0 J(\psi, q) + \frac{\partial}{\partial x}\left(K\kappa_e\frac{\partial q}{\partial x}\right) + \frac{\partial}{\partial z}\left(\kappa_e\frac{\partial q}{\partial z}\right)\right], \quad \text{(A3)}$$

$$c'(t + \Delta t) = c(t - \Delta t)$$
$$+ 2\Delta t\left[\alpha_0 J(\psi, c) + \frac{\partial}{\partial x}\left(K\kappa_e\frac{\partial c}{\partial x}\right) + \frac{\partial}{\partial z}\left(\kappa_e\frac{\partial c}{\partial z}\right)\right]. \quad \text{(A4)}$$

The final values for θ, q and c when a phase change occurs are calculated from

$$\theta(t + \Delta t) = \theta'(t + \Delta t) + \gamma\text{CD}*\text{CF}(z), \quad \text{(A5)}$$
$$q(t + \Delta t) = q'(t + \Delta t) - \text{CD}, \quad \text{(A6)}$$
$$c(t + \Delta t) = c'(t + \Delta t) + \text{CD}, \quad \text{(A7)}$$

where γ is $(L/c_p)\pi_0$ with L the latent heat of vaporization and c_p the specific heat of dry air at constant pressure. The CD is rate of condensation, and CF(z) is a coefficient that represents the probability distribution of clouds in an area defined by the grid scale of the model (usually the grid area is much larger than single clouds). This is a new modification that had been used to parameterize subgrid convection in the three-dimensional mesoscale model of Orlanski and Polinsky (1984). Then the cloud fraction, CF, can be viewed as the probability for a cloud fraction to occur at a given height. In this particular case it was found that

$$\text{CF} = 1 - (z/H) \quad \text{(A8)}$$

was quite appropriate where H is the depth of the model. This distribution implies that if moist unstable conditions occur in the model environment, one horizontal grid size of the model will have a probability

near 1.0 to be filled with clouds in the lower atmosphere with the probability dropping to 0.5 in the middle levels and 0.0 in the upper levels.

The rate of condensation, CD, is calculated as (following Lipps, 1977),

$$CD = \frac{\partial q}{\partial t} - \frac{\partial q_s}{\partial t} - \frac{q_s^{(t-\Delta t)} - q^{(t-\Delta t)}}{2\Delta t} \qquad (A9)$$

where $\partial q/\partial t$ represents the local increase in q if no condensation is present as given by Eq. (A3); $\partial q_s/\partial t$ is the rate of change of saturation mixing ratio and is given by

$$\frac{\partial q_s}{\partial t} \approx \frac{Lq_s}{R_v\theta_0^2}\frac{\partial \theta}{\partial t}. \qquad (A10)$$

This expression and the value of q_s are obtained through the Clausius–Clapeyron equation. The last finite difference terms on the right side of Eq. (A9) represent corrections when no condensation occurs at the time $(t - \Delta t)$. Since $q^{(t-\Delta t)} = q_s^{(t-\Delta t)}$ if air is saturated at the lag time step, the correction can be included for all calculations. Evaluating CD from Eqs. (A3), (A9) and (A10), one may replace the thermodynamic equation (A5) by the expression:

$$\frac{\partial \theta}{\partial t} = \frac{\left[\dfrac{\theta'^{(t+\Delta t)} - \theta^{(t-\Delta t)}}{2\Delta t} + \gamma * CF * CH\right]}{1 + \dfrac{L^2 q_s}{C_p R_v \theta_0^2}}, \qquad (A11)$$

where CH is CD plus the $\partial q_s/\partial t$ term. Inside the saturated cloud CD is calculated in the following manner: first $\partial\theta/\partial t$ is obtained from Eq. (A11), then $\partial q_s/\partial t$ is calculated from Eq. (A10), and finally CD is evaluated from Eq. (A9). At this point the final values of $\theta(t + \Delta t)$, $q(t + \Delta t)$ and $c(t + \Delta t)$ are derived from Eqs. (A5), (A6) and (A7).

The eddy viscosity formulation to be used here is adapted from the formulation first used by Orlanski and Ross (1973). The viscosity treatment in that paper involved a constant background viscosity ν_0 and a nonlinear term which was only nonzero at points where the stratification was unstable, i.e., $\theta_z < 0$.

In this paper we employ the equivalent potential temperature gradient θ_{ez} when extending the viscosity formulation to the moist case, where

$$\theta_e = \theta \exp\left(\frac{Lkq_s}{c_p\pi_0\theta}\right). \qquad (A12)$$

Hence, the viscosity will be determined by the potential temperature gradient θ_z when the air is unsaturated and by the equivalent potential temperature gradient θ_{ez} when saturation occurs. Because of this dependence upon θ_z and θ_{ez}, the viscosity formulation produces strong diffusive effects in regions which are statically unstable. In this way its effect is similar to that of convective adjustment procedures (Manabe et al., 1965)

which are frequently used in large-scale atmospheric models. However, because the present viscosity approach requires a number of time steps to adjust the unstable regions, it should be more appropriate for mesoscale models than the usual "instantaneous" convective adjustment methods.

The eddy viscosity formulation to be used here is summarized as follows:

$$\nu_e = \begin{cases} \nu_0, & \text{if } q < kq_s \text{ and } \Delta\theta \geqslant 0 \\ & \text{or } q = kq_s \text{ and } \Delta\theta_e \geqslant 0 \\ \nu_0\left\{1 + C\left[\left(\dfrac{g|\Delta\theta|(\Delta z)^3}{\theta_0\kappa_0\nu_0}\right)^{1/3}\right]\right\}, \\ & \text{if } q < kq_s \text{ and } \Delta\theta < 0 \\ \nu_0\left\{1 + C\left[\left(\dfrac{g|\Delta\theta_e|(\Delta z)^3}{\theta_0\kappa_0\nu_0}\right)^{1/3}\right]\right\}, \\ & \text{if } q = kq_s \text{ and } \Delta\theta_e < 0, \end{cases} \qquad (A13)$$

where $\Delta\theta$ and $\Delta\theta_e$ are local vertical gridpoint differences. In the moist model, $\nu_e = 0.7\kappa_e$ and $\nu_0 = 0.7\kappa_0$. The constant K included in the horizontal diffusion terms of the prognostic equations has a value of 400. Usual values of κ_0 and C are 5 m^2 s^{-1} and 0.75.

Additional conditions required for moisture variables q and c are

$$\left.\begin{array}{ll} q_{zz} = c_{zz} = 0 & \text{at } z = H \\ \bar{c}_z = 0 & \text{at } z = 0 \end{array}\right\} .$$

The boundary condition for q at $z = 0$ is similar to that of the potential temperature, θ, in the surface heating case where $q_{(z=0)}$ is fixed at a prescribed relative humidity distribution $R(x)$ such that

$$q = q_s R(x) \quad \text{at} \quad z = 0;$$

$R(x)$ has the same spatial distribution as potential temperature with constant values of 85% outside the surface heating region and 92% inside the region. The initial vertical distribution of R ranges from 85 to 80% within the mixed layer (0–2000 m), then decreases linearly to a value of 5% at the top of the model (15 km).

REFERENCES

Asai, T., 1962: Numerical experiment of convection in the model atmosphere. Proc. Int. Symp. Numerical Weather Prediction. Tokyo, *J. Meteor. Soc. Japan*, 469–476.

Blumen, W., 1979: On short wave baroclinic instability. *J. Atmos. Sci.*, **36**, 1925–1933.

——, 1980: On the evolution and interaction of short and long baroclinic waves of the Eady type. *J. Atmos. Sci.*, **37**, 1984–1993.

Bosart, L. F., 1981: The President's day snowstorm of 18–19 February 1979: A subsynoptic event. *Mon. Wea. Rev.*, **109**, 1542–1566.

——, and S. C. Lin, 1984: A diagnostic analysis of the President's day storm of February 1979. *Mon. Wea. Rev.*, **112**, 2148–2177.

Drazin, P. G., 1978: Variations on a theme of Eady. *Rotating Fluids in Geophysics*, P. H. Roberts and A. M. Soward, Eds., Academic Press, 139–169 pp.

Eady, E., 1949: Long waves and cyclonic waves. *Tellus*, **1**, (3), 33–52.

Farrell, B. F., 1982: The initial growth of disturbances in a baroclinic flow. *J. Atmos. Sci.*, **39**, 1663–1685.

Gall, R. L., 1976a: Structural changes of growing baroclinic waves. *J. Atmos. Sci.*, **33**, 374–390.

——, 1976b: The effect of released latent heat in growing baroclinic waves. *J. Atmos. Sci.*, **33**, 1686–1701.

Gambo, K., 1970: The characteristic features of medium-scale disturbances in the atmosphere (II). *J. Meteor. Soc. Japan*, **48**, 315–330.

Hart, J. E., 1979: Finite amplitude baroclinic instability. *Annual Reviews in Fluid Mechanics*, Vol. 11, Annual Reviews, 147–172.

Held, I. M., 1982: The height of the tropopause and the static stability of the troposphere. *J. Atmos. Sci.*, **39**, 412–417.

Hoskins, B. J., and F. P. Bretherton, 1972: Atmospheric frontogenesis models: Mathematical formulation and solution. *J. Atmos. Sci.*, **29**, 11–37.

——, and N. V. West, 1979: Baroclinic waves and frontogenesis. Part II. Uniform potential vorticity jet flows—cold and warm fronts. *J. Atmos. Sci.*, **36**, 1663–1680.

Lipps, F. B., 1977: A study of turbulence parameterization in a cloud model. *J. Atmos. Sci.*, **34**, 1751–1772.

Manabe, S., J. Smagorinsky and R. F. Strickler, 1965: Simulated climatology of a general circulation model with a hydrologic cycle. *Mon. Wea. Rev.*, **93**, 769–798.

Mullen, S. L., 1979: An investigation of small synoptic-scale cyclones in polar air streams. *Mon. Wea. Rev.*, **107**, 1636–1647.

——, 1983: Explosive cyclogenesis associated with cyclones in polar streams. *Mon. Wea. Rev.*, **111**, 1537–1553.

Nitta, T., and Y. Ogura, 1972: Numerical simulation of the development of the intermediate-scale cyclone in a moist model atmosphere. *J. Atmos. Sci.*, **29**, 1011–1024.

Orlanski, I., and M. D. Cox, 1973: Baroclinic instability in ocean currents. *Geophys. Fluid Dyn.*, **4**, 297–332.

——, and B. B. Ross, 1973: Numerical simulation of the generation and breaking of internal gravity waves: Part I. *J. Geophys. Res.*, **78**, 8808–8826.

——, and ——, 1977: The circulation associated with a cold front. Part I: Dry case. *J. Atmos. Sci.*, **34**, 1619–1633.

——, and L. J. Polinsky, 1983: Ocean response to mesoscale atmospheric forcing. *Tellus*, **35A**, 296–323.

——, and ——, 1984: Predictability of mesoscale phenomena. *Proc. Int. Symp. Nowcasting, 2nd*, Norrköping, Sweden, pp. 271–280.

——, L. J. Polinsky and R. Shaginaw, 1985: Advances in the theory of atmospheric fronts. *Issues in Atmospheric and Oceanic Modeling*, S. Manabe, Ed., Academic Press, 223–252.

Pedlosky, J., 1970: Finite amplitude baroclinic waves. *J. Atmos. Sci.*, **27**, 15–30.

Phillips, N. A., 1954: Energy transformations and meridional circulations associated with simple baroclinic waves in a two-level, quasi-geostrophic model. *Tellus*, **6**, 273–286.

——, 1964: An overlooked aspect of the baroclinic stability problem. *Tellus*, **16**, 268–270.

Rasmussen, E., 1979: The polar low as an extratropical CISK-disturbance. *Quart. J. Roy. Meteor. Soc.*, **105**, 531–549.

——, 1981: An investigation of a polar low with a spiral cloud structure. *J. Atmos. Sci.*, **38**, 1785–1792.

Reed, R. J., 1979: Cyclogenesis in polar air streams. *Mon. Wea. Rev.*, **107**, 38–52.

Ross, B. B., and I. Orlanski, 1978: The circulation associated with a cold front. Part II: Moist case. *J. Atmos. Sci.*, **35**, 445–465.

Sanders, F., and J. R. Gyakum, 1980: Synoptic–dynamic climatology of the "Bomb." *Mon. Wea. Rev.*, **108**, 1589–1606.

Staley, D. O., and R. L. Gall, 1977: On the wavelength of maximum baroclinic instability. *J. Atmos. Sci.*, **34**, 1679–1688.

Stone, P. H., 1970: On non-geostrophic baroclinic stability: Part II. *J. Atmos. Sci.*, **27**, 721–726.

Takeda, T., 1965: The downdraft in convective shower-cloud under the vertical wind shear and its significance for the maintenance of convective system. *J. Meteor. Soc. Japan*, **43**, 302–309.

——, 1971: Numerical simulation of a precipitating convective cloud: The formation of a "long lasting" cloud. *J. Atmos. Sci.*, **28**, 350–376.

Uccellini, L. F., P. J. Kocin, R. A. Petersen, C. H. Wash and K. F. Brill, 1984: The President's Day cyclone of 18–19 February 1979: Synoptic overview and analysis of the subtropical jet streak influencing the pre-cyclogenetic period. *Mon. Wea. Rev.*, **112**, 31–55.

Williams, R. T., 1967: Atmospheric frontogenesis: A numerical experiment. *J. Atmos. Sci.*, **24**, 627–641.